Journal of Computational Physics 328 (2017) 234–257

Contents lists available at ScienceDirect

Journal of Computational Physics

www.elsevier.com/locate/jcp

A numerical study on parasitic capillary waves using unsteady conformal mapping

Sunao Murashige [a,*], Wooyoung Choi [b]

[a] Department of Mathematics and Informatics, Ibaraki University, Mito, Ibaraki, 310-8512, Japan
[b] Department of Mathematical Sciences, New Jersey Institute of Technology, Newark, NJ 07102-1982, USA

ARTICLE INFO

Article history:
Received 26 January 2016
Received in revised form 7 September 2016
Accepted 5 October 2016
Available online 12 October 2016

Keywords:
Gravity-capillary water waves
Unsteady hodograph transformation
Conformal mapping
Fully nonlinear computation
Numerical stability

ABSTRACT

This paper describes fully nonlinear computation of unsteady motion of parasitic capillary waves that appear on the front face of steep gravity waves progressing on water of infinite depth, within the framework of irrotational plane flow. As an alternative to the widely-used boundary integral method with mixed-Eulerian–Lagrangian (MEL) time updating, we focus on a numerical method based on unsteady conformal mapping, which will be hereafter referred to as the unsteady hodograph transformation (UHT) method. In this method, we solve the nonlinear evolution equations to find an unsteady conformal map in a complex plane with which the flow domain is mapped onto the unit disk while the free surface is fixed on the unit circle. The aim of this work is to compare the UHT method with the MEL method and find a more efficient method to compute parasitic capillary waves. From linear stability analysis, it is found that a critical difference between these two methods arises from the kernel of cotangent function in singular integrals, and the UHT method can avoid some numerical instability due to it. Numerical examples demonstrate that the UHT method is more suitable than the MEL method for not only parasitic capillary waves, but also capillary dominated waves. In particular, the UHT method requires no artificial techniques, such as filtering, to control numerical errors, in these examples. In addition, another major difference between the two methods is observed in terms of the clustering property of sample points on the free surface, depending on the restoring force of waves (gravity or surface tension).

1. Introduction

We consider numerical computation of “parasitic capillary waves”, which are a train of short capillary waves generated on the forward face of steep gravity waves progressing on water of infinite depth. These waves have been studied extensively as they play important roles in the generation of wind waves and wave breaking (see review by Perlin & Schultz [39]). In addition, the complete understanding of parasitic capillary waves is necessary for accurate estimation of sea state from remote sensing of the sea surface elevation.

Since Cox’s experiments [14], considerable progress has been made in the study of parasitic capillary waves. Longuet-Higgins [30,31] developed a linear steady model with viscous damping by assuming that the parasitic capillary waves can be considered as a perturbation due to surface tension on progressive pure gravity waves. His theory agrees qualitatively with

* Corresponding author.
E-mail addresses: sunao.murashige.sci@vc.ibaraki.ac.jp (S. Murashige), wychoi@njit.edu (W. Choi).

http://dx.doi.org/10.1016/j.jcp.2016.10.015

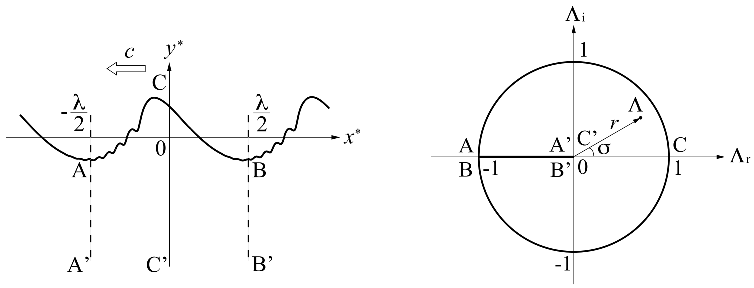

(a) The physical plane $(z = x + \mathrm{i}y)$

(b) The Λ-plane $(\Lambda = \Lambda_\mathrm{r} + \mathrm{i}\Lambda_\mathrm{i} = r\mathrm{e}^{\mathrm{i}\sigma})$

Fig. 1. The two-dimensional motion of periodic water waves in the frame of reference moving with waves and conformal mapping of the flow domain onto the unit disk in the Λ-plane. The coordinates x^* and y^* are non-dimensionalized as $x = (2\pi/\lambda)x^*$ and $y = (2\pi/\lambda)y^*$ (see eq. (1)). c and λ are characteristic speed and length of waves, respectively.

some experiments [14,22,38]. Some additional effects such as wind forcing [23,24] or vortex motion [34,27] have also been considered. However, as Jiang et al. [28] remarked, the essential mechanism of generation of parasitic capillary waves is the nonlinear interaction between short capillary waves and long gravity waves in an inviscid flow. Also, while the steadiness assumption has been often adopted [30,31,23,24], the flow unsteadiness is non-negligible [19,28].

In this work, to catch this nonlinear and unsteady process, we focus on fully nonlinear computation of unsteady motion of gravity-capillary waves within the framework of irrotational plane flow in the vertical cross-section along the propagation direction of waves, as shown in Fig. 1(a). Here it should be noted that our main interest is in the generation and growth of capillary waves on primary gravity waves, which is essentially different from finding steady and symmetric solutions of gravity-capillary waves considered by Schwartz & Vanden-Broeck [42] and Chen & Saffman [10,11].

As a standard method of fully nonlinear computation of unsteady water waves, a boundary integral method with mixed-Eulerian–Lagrangian time updating has been well developed [50,1,18,4,40,26,3] (see reviews by Hou [25], Tsai & Yue [48], Dias & Bridges [17] and Perlin, Choi & Tian [37]) after Longuet-Higgins & Cokelet [32] proposed the method for two-dimensional breaking waves. This method is based on a boundary integral formulation for fully nonlinear potential flow problems with time updating using the free surface conditions in a mixed-Eulerian–Lagrangian form (eqs. (7) and (8) in section 2.1). We call this method the mixed-Eulerian–Lagrangian (MEL) method or just “MEL”. Validity of the MEL method has been examined experimentally [20,44] and theoretically [4,5,8]. Jiang et al. [28] applied this method to parasitic capillary waves, and found that nonlinearity and unsteadiness characterize this phenomenon. However, Beale et al. [5] and Hou [25] pointed out that the numerical simulations using this method are sensitive to numerical instabilities due to discretization of a singular integral and aliasing errors, as will be also discussed in sections 4.1 and 5.1 of this paper. Although a number of variations exist for MEL, we choose for our computation the approach of Beale et al. [4,5,25], whose numerical properties have been extensively studied.

Recently an alternative approach via time-dependent conformal mapping has been used to fully nonlinear computation of the two-dimensional motion of water waves [33,9,13,21,29,12,47] (see the review by Perlin, Choi & Tian [37, section 6.1]). In this method, the flow domain is conformally mapped onto a fixed domain such as a strip of uniform thickness or a unit disk in a complex plane, and the free surface is onto its boundary that remains unchanged in time, as shown in Fig. 1(b). The time-dependent conformal mapping functions and, therefore, the time evolution of the free surface in the physical plane can be determined by solving the surface Euler equations given later by eqs. (9) and (10) in section 2.2. We call this method the Unsteady Hodograph Transformation (UHT) method or just “UHT” as the formulation in the steady limit can be reduced to the classical hodograph transformation commonly used for steady waves, where the fluid domain is mapped into a uniform strip or a unit disk by interchanging the roles of dependent and independent variables.

It should be noticed that Longuet-Higgins & Cokelet [32] and Schultz, Huh & Griffin [40] also combined a conformal mapping technique with MEL to study breaking gravity waves. In their method, the still water level is mapped onto the unit circle using a stationary or time-independent mapping function, and the free surface moves in time in the mapped complex plane. On the other hand, in UHT, the whole flow domain is conformally mapped onto the unit disk using a non-stationary mapping function so that the free surface always stays on the unit circle in the mapped plane. Thus, evaluating a singular integral written in the mapped plane in UHT is much simpler than that in the physical plane in MEL, as shown in section 5.2. Also note that Tanveer [45,46] discussed time variation of singularities of a solution by conformally mapping the flow domain onto the unit disk and using analytic continuation of the free surface conditions.

In both methods, MEL and UHT, each dependent variable and its spatial derivative are spectrally estimated under periodic boundary conditions via a pseudo-spectral method based on Fast Fourier transform (FFT). Then, due to spectral approximation using finite Fourier series, aliasing errors are unavoidable when nonlinear problems are solved, as shown in section 3.1. Nevertheless, the UHT method has some advantages in reducing these numerical errors, as demonstrated in section 6. Therefore, in comparison with the MEL method, the UHT method is shown more suitable for capillary dominated flows, as discussed in section 7. Earlier Chalikov and Sheinin [9] simulated overturning of gravity waves using the UHT method with dissipation and redistributing sample points. Here we use the formulation described in section 2.2, which is more numerically stable without dissipation or any artificial techniques to control numerical errors, as shown in section 4.2.

This paper is organized as follows. The basic formulations for the two computational methods, MEL and UHT, are presented in section 2. Approximations of spatial derivatives and singular integrals in the two methods are summarized in section 3. Numerical stability of the two methods is linearly analyzed in section 4. Using the numerical methods for the two methods summarized in section 5, the computed results are presented in Section 6 for pure gravity waves, pure capillary waves, and parasitic capillary waves. Section 7 discusses the difference between the two methods from the point of view of spatial resolution on the free surface. Section 8 concludes this paper.

2. Formulation of the two methods of computation

Assume that the flow is irrotational and that the fluid is incompressible and inviscid. Consider the two-dimensional fully nonlinear and unsteady motion of periodic gravity-capillary waves on deep water in the vertical cross-section (x, y) along the propagation direction, as shown in Fig. 1(a). In this section, we summarize two computational methods, MEL and UHT, for this problem. It is convenient to formulate the problem in the flow domain for one period with wavelength λ, namely the domain surrounded by ACBB′C′A′ in Fig. 1(a), in the frame of reference moving to the left with waves.

For irrotational plane flows, we can introduce the complex coordinate $z = x + \mathrm{i}y$ and the complex velocity potential $f = \phi + \mathrm{i}\psi$, where ϕ and ψ denote the velocity potential and the stream function, respectively. With characteristic wave speed c and wavelength λ, all physical variables are non-dimensionalized as follows:

$$z = \frac{2\pi}{\lambda} z^* \,, \quad f = \frac{2\pi}{c\lambda} f^* \,, \quad w = \frac{1}{c} w^* \quad \text{and} \quad t = \frac{2\pi c}{\lambda} t^* \,, \tag{1}$$

where a variable with superscript * denotes a dimensional one, $w = \partial f/\partial z = u - \mathrm{i}v$ is the complex velocity, and t is the time. Note that the complex coordinate Z and the complex velocity potential F in the inertial frame are related to z and f in the moving frame by

$$Z = z - t \quad \text{and} \quad F = f - z \ . \tag{2}$$

The problem of gravity-capillary waves on deep water is determined by two non-dimensional parameters, the Froude number F_λ and the Weber number W_e, defined by

$$F_\lambda = \frac{c}{\sqrt{g\lambda}} \quad \text{and} \quad W_e = \frac{\varrho c^2 \lambda}{T} \ , \tag{3}$$

where g is the gravitational acceleration, ϱ is the density of fluid, and T is the surface tension.

2.1. The MEL method

The MEL method has been improved for many years and there are a number of variant formulations. Here, for a fair comparison with the straightforward UHT method, we adopt the relatively simple formulation proposed by Beale et al. in [4,5,25], for which some fundamental properties such as convergence or stability have been well studied. This method is based on the following two basic ideas:

(i) The free surface can be parametrized using the Lagrangian coordinate α as $z = z(\alpha, t)$, where α ranges from $-\pi$ to π for one periodic wave motion.

(ii) The complex velocity potential $f = f(\alpha, t)$ on the free surface is expressed using the double layer representation with the dipole strength $\mu(\alpha, t)$ and 2π-periodicity in α as

$$\begin{aligned} f(\alpha,t) &= z(\alpha,t) + \frac{\mu(\alpha,t)}{2} + \frac{1}{2\pi \mathrm{i}} \mathrm{P.V.}\int_{-\infty}^{\infty} \mu(\alpha',t) \frac{z_\alpha(\alpha',t)}{z(\alpha,t) - z(\alpha',t)} \mathrm{d}\alpha' \\ &= z(\alpha,t) + \frac{\mu(\alpha,t)}{2} \\ &\quad + \frac{1}{4\pi \mathrm{i}} \mathrm{P.V.}\int_{-\pi}^{\pi} \mu(\alpha',t) z_\alpha(\alpha',t) \cot\left(\frac{z(\alpha,t) - z(\alpha',t)}{2}\right) \mathrm{d}\alpha' \ , \end{aligned} \tag{4}$$

as shown in [1, eq. (2.3)]. Taking differentiation of (4) with respect to α and integrating by parts, we get

$$\begin{aligned} f_\alpha(\alpha,t) &= z_\alpha(\alpha,t) + \frac{\gamma(\alpha,t)}{2} \\ &\quad - \frac{z_\alpha(\alpha,t)}{4\pi \mathrm{i}} \mathrm{P.V.} \int_{-\pi}^{\pi} \mu(\alpha',t) \frac{z_\alpha(\alpha',t)}{2} \operatorname{cosec}^2\left(\frac{z(\alpha,t)-z(\alpha',t)}{2}\right) \mathrm{d}\alpha' \\ &= z_\alpha(\alpha,t) + \frac{\gamma(\alpha,t)}{2} \\ &\quad + \frac{z_\alpha(\alpha,t)}{4\pi \mathrm{i}} \mathrm{P.V.} \int_{-\pi}^{\pi} \gamma(\alpha',t) \cot\left(\frac{z(\alpha,t)-z(\alpha',t)}{2}\right) \mathrm{d}\alpha' \ , \end{aligned} \tag{5}$$

with

$$\gamma(\alpha,t) = \mu_\alpha(\alpha,t) \ , \tag{6}$$

where P.V. denotes Cauchy's principal value and the subscript α represents the partial differentiation with respect to α. Equation (5) corresponds to eq. (3) in [4].

In this method, $z = z(\alpha,t)$ and $\phi = \phi(\alpha,t)$ are two dependent variables, whose evolutions are governed by the kinematic free surface boundary condition

$$\frac{\partial \bar{z}}{\partial t}(\alpha,t) = w(\alpha,t) = \frac{f_\alpha}{z_\alpha} \ , \tag{7}$$

and the dynamic free surface boundary condition

$$\frac{\partial \phi}{\partial t} = \frac{1}{2}(u^2+v^2) + \frac{1}{2} - \frac{1}{2\pi {F_\lambda}^2}\, y + \frac{2\pi}{W_e} \frac{y_{\alpha\alpha}x_\alpha - x_{\alpha\alpha}y_\alpha}{({x_\alpha}^2+{y_\alpha}^2)^{3/2}} \ , \tag{8}$$

where $\bar{z}$ is the complex conjugate of z and $u^2+v^2 = |w|^2$.

One should notice that, as α in MEL is the Lagrangian parameter such that z for a given value of α represents the location of a fluid particle, the partial time derivatives in (7) and (8) are equivalent to the material derivative in the Eulerian description. Equations (7) and (8) are called the free surface conditions in a mixed-Eulerian–Lagrangian form [17, p. 807].

The algorithm of MEL can be summarized as follows:

Step 1. Set the initial values of z and ϕ.
Step 2. Substitute z and ϕ into the real part of the integral equation (4) (or (5)), and obtain μ (or γ).
Step 3. Substitute μ (or γ) into (4) (or (5)), and obtain f_α and $w = f_\alpha/z_\alpha$.
Step 4. Substitute z and w into the right hand side of (7) and (8), and update z and ϕ in time t. Then, go back to Step 2.

2.2. The UHT method

In the UHT method, the flow domain is conformally mapped onto a unit disk $|\Lambda| < 1$ in the Λ-plane, where the free surface is mapped for all t onto the unit circle $\Lambda = \mathrm{e}^{\mathrm{i}\sigma}$ $(-\pi \le \sigma \le \pi)$ with the branch cut along the negative real axis in the Λ-plane, as shown in Fig. 1(b). In this method, the mapping function between the z- and Λ-plane is unknown and determined as a solution $z = z(\Lambda,t)$ with $f = f(\Lambda,t)$ such that both of them satisfy initial and boundary conditions, as shown in section 5.2. Then $y = y(\sigma,t)$ and $\phi = \phi(\sigma,t)$ on the free surface $\Lambda = \mathrm{e}^{\mathrm{i}\sigma}$ and we choose them as dependent variables. The evolution equations of these variables are given by the kinematic free surface boundary condition:

$$\frac{\partial y}{\partial t} = -x_\sigma \frac{1}{{s_\sigma}^2}\psi_\sigma + y_\sigma \cdot \mathcal{H}\left[\frac{1}{{s_\sigma}^2}\psi_\sigma\right] \ , \tag{9}$$

and the dynamic free surface boundary condition:

$$\frac{\partial \phi}{\partial t} = \phi_\sigma \cdot \mathcal{H}\left[\frac{1}{{s_\sigma}^2}\psi_\sigma\right] - \frac{1}{2{s_\sigma}^2}({\phi_\sigma}^2 - {\psi_\sigma}^2) + \frac{1}{2} - \frac{1}{2\pi {F_\lambda}^2} y - \frac{2\pi}{W_e}\frac{y_{\sigma\sigma}x_\sigma - x_{\sigma\sigma}y_\sigma}{{s_\sigma}^3} \ , \tag{10}$$

where

$$s_\sigma = \sqrt{{x_\sigma}^2 + {y_\sigma}^2} \ , \tag{11}$$

and $\mathcal{H}$ is the Hilbert transform for a 2π-periodic function φ defined by

$$\mathcal{H}[\varphi(\sigma,t)] = \frac{1}{2\pi}\text{P.V.}\int_{-\pi}^{\pi} \varphi(\sigma',t)\cot\left(\frac{\sigma-\sigma'}{2}\right)\mathrm{d}\sigma' \ . \tag{12}$$

Derivation of (9) and (10) can be found in [36,13,21]. Note that the corresponding equations in [36,13,21] (for example [13, eqs. (34) and (35) in p. 758]) are obtained in another complex plane, the ζ $(=\xi+\mathrm{i}\eta)$-plane, where the flow domain is mapped onto a semi-infinite strip $-\xi_1/2 \le \xi \le \xi_1/2$ and $\eta \le 0$ for periodic waves on deep water. This strip in the ζ-plane can be mapped onto the unit disk in the Λ-plane using $\Lambda = \mathrm{e}^{-\mathrm{i}2\pi\zeta/\xi_1}$, in particular $-2\pi\xi/\xi_1 = \sigma$ on the free surface $\zeta = \xi$ or $\Lambda = \mathrm{e}^{\mathrm{i}\sigma}$, and thus transformation of the free surface conditions in the ζ-plane into those in the Λ-plane is straightforward. We call these two equations (9) and (10) the "surface Euler equations" [29] that determine the time evolution of the free surface and the velocity potential evaluated at the free surface. Using analyticity of $\partial z/\partial f = 1/w$ in the Λ-plane, we can obtain x_σ and ψ_σ in the right-hand side of (9) and (10) from y and ϕ, respectively, as shown in section 5.2.

The algorithm of the UHT method can be summarized as follows:

Step 1. Set the initial values of y and ϕ.

Step 2. Using analyticity of $\partial z/\partial f$, determine x_σ and ψ_σ from y and ϕ, respectively (see section 5.2).

Step 3. Substitute y, ϕ, x_σ and ψ_σ into the right hand side of (9) and (10), and update y and ϕ in time t. Then, go back to Step 2.

3. Approximations of dependent variables and singular integrals

3.1. Spectral estimation of dependent variables with filtering

We consider 2π-periodic variable $y(\alpha,t) = y(\alpha+2\pi,t)$ for $-\pi \le \alpha \le \pi$, which can be approximated in the MEL method by

$$y(\alpha,t) \simeq \sum_{k=-N/2}^{N/2-1} \hat{y}_k(t)\mathrm{e}^{\mathrm{i}k\alpha} \quad \text{with } \hat{y}_k(t) = \frac{1}{N}\sum_{j=0}^{N-1} y(\alpha_j,t)\mathrm{e}^{-\mathrm{i}k\alpha_j} \ , \tag{13}$$

where $\hat{y}_k$'s are the approximate Fourier coefficients of $y(\alpha,t)$ and α_j $(j = 0,1,\cdots,N-1)$ are the discretized points of α $(-\pi \le \alpha \le \pi)$. The Fourier coefficients $\hat{y}_k$'s are determined numerically using a pseudo-spectral method with fast Fourier transform (FFT) from the discretized data $y(\alpha_j,t)$ $(j = 0,1,\cdots,N-1)$. The similar approximations are applied to $y(\sigma,t)$ in the UHT method and all other variables in the two numerical methods. For the use of FFT, we assume N to be powers of 2, and discretize α in MEL with an equal interval as

$$\alpha_j = -\pi + j\cdot\Delta\alpha \quad \text{with } \Delta\alpha = 2\pi/N \quad (j = 0,1,\cdots,N) \ , \tag{14}$$

and, similarly, σ in UHT as

$$\sigma_j = -\pi + j\cdot\Delta\sigma \quad \text{with } \Delta\sigma = 2\pi/N \quad (j = 0,1,\cdots,N) \ . \tag{15}$$

Then, a spatial derivative y_α can be approximated by

$$y_\alpha(\alpha,t) \simeq \sum_{k=-N/2}^{N/2-1} \mathrm{i}k\hat{y}_k(t)\mathrm{e}^{\mathrm{i}k\alpha} =: D_\alpha y(\alpha,t) \ . \tag{16}$$

Here it should be remarked that, from periodicity, the approximate Fourier coefficients $\hat{y}_k$'s are related to the exact ones $\check{y}_k$'s by the aliasing law [7, eq. (2.1.29)]

$$\hat{y}_k = \check{y}_k + \sum_{\substack{m=-\infty \\ m\neq 0}}^{\infty} \check{y}_{k+mN} \quad \text{where } \ \check{y}_k = \frac{1}{2\pi}\int_{-\pi}^{\pi} y(\alpha',t)\mathrm{e}^{-\mathrm{i}k\alpha'}\mathrm{d}\alpha' \ . \tag{17}$$

This difference between $\hat{y}_k$ and $\check{y}_k$ makes the two numerical methods suffer from the aliasing error, in addition to the truncation error introduced by finite Fourier series given by (13). To reduce the aliasing and round-off errors, various filtering techniques have been proposed, in particular, in evaluating spatial derivatives [6,7]. In this work, if necessary, we also apply a filter for spatial derivatives as

$$y_\alpha(\alpha,t) \simeq \sum_{k=-N/2}^{N/2-1} \mathrm{i}k\rho(k)\hat{y}_k(t)\mathrm{e}^{\mathrm{i}k\alpha} =: D_\alpha^{(\rho)} y(\alpha,t) \ , \tag{18}$$

where the Fourier coefficients in (16) are artificially controlled using a filtering function $\rho(k)$ with $0 < \rho \le 1$.

We should remark that the straightforward application of some dealiasing techniques without care could produce erroneous results, as pointed out by Boyd in [6, Chapter 11]. He emphasizes that, if the flow is well-resolved and the scheme is stable, the spectral method might not need any dealiasing techniques. It is in fact shown in section 6 that, when compared with MEL, the UHT method is more stable and produces accurate solutions without any dealiasing techniques.

3.2. Approximation of singular integrals

We need to estimate singular integrals in both numerical methods. In MEL, the singular integral in the double layer representation (4) or (5) can be approximated using the alternating trapezoidal rule given by

$$\begin{aligned} I(\alpha_j) &= \mathrm{P.V.}\int_{-\pi}^{\pi} \varphi(\alpha')\cot\left(\frac{z(\alpha_j)-z(\alpha')}{2}\right)\mathrm{d}\alpha' \\ &\simeq \sum_{\substack{k=0\\(k-j)\mathrm{odd}}}^{N-1} \varphi(\alpha_k)\cot\left(\frac{z(\alpha_j)-z(\alpha_k)}{2}\right)\cdot 2\Delta\alpha \ , \end{aligned} \tag{19}$$

where the time t is omitted such as $z(\alpha_j)=z(\alpha_j,t)$. Here note that, for a periodic function $\varphi(\alpha)$, this approximation is spectrally accurate [43], as emphasized by Beale et al. [4, p. 1803].

On the other hand, for the singular integral in UHT, namely the Hilbert transform (12), we have the exact relation given by

$$\mathcal{H}[\mathrm{e}^{\mathrm{i}k\sigma}] = -\mathrm{i}\,\mathrm{sgn}(k)\mathrm{e}^{\mathrm{i}k\alpha} \quad \text{for } k\in\mathbb{Z} \quad \text{with } \mathrm{sgn}(k)=\begin{cases} +1 & (k=1,2,\cdots) \\ -1 & (k=-1,-2,\cdots) \\ \ \ 0 & (k=0) \end{cases} \tag{20}$$

Note that $\mathrm{sgn}(k=0)=0$ and $\mathcal{H}[1]=0$. Using this relation, the Hilbert transform for a 2π-periodic function $\varphi(\sigma,t)$ can be approximated as

$$\mathcal{H}[\varphi(\sigma,t)] \simeq \mathcal{H}\left[\sum_{k=-N/2}^{N/2-1}\hat{\varphi}_k(t)\mathrm{e}^{\mathrm{i}k\sigma}\right] = -\mathrm{i}\sum_{k=-N/2}^{N/2-1}\mathrm{sgn}(k)\hat{\varphi}_k(t)\mathrm{e}^{\mathrm{i}k\alpha} \ , \tag{21}$$

where $\hat{\varphi}_k(t)$ is the approximate Fourier coefficients given by (16).

It should be noticed that the cotangent function in the integrand of the singular integral in MEL is different from that in UHT. Namely, the cotangent function in MEL is written in terms of the dependent variable $z(\alpha,t)$, but the same function in UHT is written in terms of the independent variable σ and is independent of time. This difference is intimately related to the difference of numerical stability of the two methods, as shown in section 4.

In addition, similarly to Baker et al. [1, p. 483] and Baker & Xie [3, p. 91], singularity of the integrand in the last term of (5) in MEL can be removed as

$$\begin{aligned} &\frac{z_\alpha(\alpha,t)}{4\pi\mathrm{i}}\mathrm{P.V.}\int_{-\pi}^{\pi}\gamma(\alpha',t)\cot\left(\frac{z(\alpha,t)-z(\alpha',t)}{2}\right)\mathrm{d}\alpha' \\ &= \frac{1}{4\pi\mathrm{i}}\int_{-\pi}^{\pi}\{z_\alpha(\alpha,t)\gamma(\alpha',t)-z_\alpha(\alpha',t)\gamma(\alpha,t)\}\cot\left(\frac{z(\alpha,t)-z(\alpha',t)}{2}\right)\mathrm{d}\alpha' \ , \end{aligned} \tag{22}$$

using

$$\mathrm{P.V.}\int_{-\pi}^{\pi} z_\alpha(\alpha',t)\cot\left(\frac{z(\alpha,t)-z(\alpha',t)}{2}\right)\mathrm{d}\alpha' = 0 \ . \tag{23}$$

However we could not find any noticeable differences between the left and right hand side in (22) in some computed results under the conditions of numerical examples in section 6. In this paper, the results using (5) with (19) are shown.

4. Linear stability analysis

In this section, we examine numerical stability of the two methods, MEL and UHT, using linear stability analysis around an equilibrium state, which corresponds to a trivial solution with a flat free surface. In this equilibrium state, $y(\alpha,t)=0$

or $y(\sigma, t) = 0$ and $w = \partial f/\partial z = 1$. For stability analysis, in both methods, it is assumed that the spatial derivatives are approximated using the spectral derivative $D_\alpha^{(\rho)}$ or $D_\sigma^{(\rho)}$ defined by (18) with a filtering function $\rho(k)$. Notice that the unfiltered case is recovered by setting $\rho = 1$.

It should be remarked that the filter $\rho(k)$ was introduced originally in [4,5] to remove truncation errors associated with, for example, finite difference approximation of spatial derivatives. Even though we evaluate spatial derivatives with spectral accuracy, we apply filter to control aliasing errors if necessary.

Also note that linear stability around a flat free surface is examined as a simple case for comparison of the two methods, while Beale et al. [4] and Ceniceros & Hou [8] performed a systematic stability analysis for their discrete scheme based on the MEL boundary integral method around an arbitrary wave profile and proved nonlinear stability.

4.1. The MEL method

While Beale et al. [4], [5, Section 4] and Hou [25, Section 3.2] investigated numerical stability of the MEL boundary integral method in detail, we summarize their result to compare with that of UHT to be presented next. The solutions for z, f and μ perturbed around their equilibrium can be expressed as

$$\begin{cases} z(\alpha,t) \;=\; t+\alpha+\tilde{z}(\alpha,t) \ , \\ f(\alpha,t) \;=\; z(\alpha,t)+\frac{1}{2}+\tilde{f}(\alpha,t) \ , \\ \mu(\alpha,t) \;=\; 1+\tilde{\mu}(\alpha,t) \ , \end{cases} \tag{24}$$

where $\tilde{z}(\alpha,t)$, $\tilde{f}(\alpha,t)$, $\tilde{\mu}(\alpha,t)$ are the perturbed quantities of $\mathrm{O}(\epsilon)$ and ϵ is a small parameter measuring the wave steepness. Substituting these into the kinematic condition (7) and using (5), we obtain

$$\begin{aligned} \overline{\tilde{z}}_t \;&=\; \tilde{f}_\alpha + \mathrm{O}(\epsilon^2) \\ &=\; \frac{\tilde{\mu}_\alpha}{2} + \frac{1}{4\pi \mathrm{i}}\mathrm{P.V.}\int_{-\pi}^{\pi} \tilde{\mu}_\alpha(\alpha',t)\cot\left(\frac{\alpha-\alpha'}{2}\right)\mathrm{d}\alpha' + \mathrm{O}(\epsilon^2) \ , \end{aligned} \tag{25}$$

and thus

$$\tilde{y}_t = \frac{1}{2}\mathcal{H}[\tilde{\mu}_\alpha] + \mathrm{O}(\epsilon^2) \ . \tag{26}$$

The dynamic condition (8) can be linearized as

$$\tilde{\phi}_t = -\frac{1}{2\pi {F_\lambda}^2}\tilde{y} + \frac{2\pi}{W_e}\tilde{y}_{\alpha\alpha} + \mathrm{O}(\epsilon^2) \ . \tag{27}$$

Linearizing the double layer representation (4) for ϕ yields the relation among $\tilde{\mu}$, $\tilde{y}$, and $\tilde{\phi}$ as follows:

$$\begin{aligned} \tilde{\phi}(\alpha,t) \;&=\; \frac{\tilde{\mu}(\alpha,t)}{2} + \frac{1}{4\pi}\mathrm{P.V.}\int_{-\pi}^{\pi}\tilde{y}_\alpha(\alpha',t)\cot\left(\frac{\alpha-\alpha'}{2}\right)\mathrm{d}\alpha' \\ &\quad - \frac{1}{4\pi}\mathrm{P.V.}\int_{-\pi}^{\pi}\left(\frac{\tilde{y}(\alpha,t)-\tilde{y}(\alpha',t)}{2}\right)\mathrm{cosec}^2\left(\frac{\alpha-\alpha'}{2}\right)\mathrm{d}\alpha' + \mathrm{O}(\epsilon^2) \\ &=\; \frac{\tilde{\mu}(\alpha,t)}{2} + \frac{1}{2}\{\mathcal{H}[\tilde{y}_\alpha] - \mathcal{G}[\tilde{y}]\} + \mathrm{O}(\epsilon^2) \ , \end{aligned} \tag{28}$$

where $\mathcal{H}$ is the Hilbert transform defined by (12) and

$$\mathcal{G}[\tilde{y}] := \frac{1}{2\pi}\mathrm{P.V.}\int_{-\pi}^{\pi}\left(\frac{\tilde{y}(\alpha,t)-\tilde{y}(\alpha',t)}{2}\right)\mathrm{cosec}^2\left(\frac{\alpha-\alpha'}{2}\right)\mathrm{d}\alpha' \ . \tag{29}$$

Here we have used

$$\begin{aligned} &\cot\left(\frac{z(\alpha,t)-z(\alpha',t)}{2}\right) \\ &= \cot\left(\frac{\alpha-\alpha'}{2}\right) - \left(\frac{\tilde{z}(\alpha,t)-\tilde{z}(\alpha',t)}{2}\right)\mathrm{cosec}^2\left(\frac{\alpha-\alpha'}{2}\right) + \mathrm{O}(\epsilon^2) \ . \end{aligned} \tag{30}$$

Eliminating $\tilde{\mu}$ in (26), (27), and (28), we obtain the following linearized equations

$$\begin{cases} \dfrac{\partial \tilde{y}}{\partial t} = \mathcal{H}[\tilde{\phi}_\alpha] - \dfrac{1}{2}\mathcal{H}\left[\partial_\alpha\{\mathcal{H}[\tilde{y}_\alpha] - \mathcal{G}[\tilde{y}]\}\right] \ , \\ \dfrac{\partial \tilde{\phi}}{\partial t} = -\dfrac{1}{2\pi {F_\lambda}^2}\tilde{y} + \dfrac{2\pi}{W_e}\tilde{y}_{\alpha\alpha} \ . \end{cases} \tag{31}$$

Note that, for the singular integral operators $\mathcal{H}$ in (12) and $\mathcal{G}$ in (29), we have the exact relations (20) and

$$\mathcal{G}[\mathrm{e}^{\mathrm{i}k\alpha}] = |k|\mathrm{e}^{\mathrm{i}k\alpha} \quad \text{for } k \in \mathbb{Z} \ . \tag{32}$$

Therefore, under the spectral approximation of $\tilde{y}(\alpha, t)$ given by (13), the term from the singular integral in (31), $\mathcal{H}[\tilde{y}_\alpha] - \mathcal{G}[\tilde{y}]$, vanishes. Then, it can be shown that the linear system given by (31) is neutrally stable. Unfortunately, as discussed later, the MEL method is found numerically unstable for nonlinear computations although the UHT method is found stable under the same time-integration scheme. Therefore, to control such instability without modifying the time integration scheme for a fair comparison with UHT, a filtering function $\rho(k)$ is applied. In particular, to suppress the growth of large k or high wave number disturbances, the spatial derivatives must be controlled.

As pointed out by Beale et al. [4,5], if we apply a filtering function $\rho(k)$ to approximate only the spatial derivatives of $\tilde{y}(\alpha, t)$ and $\tilde{\phi}(\alpha, t)$ using $D_\alpha^{(\rho)}$ in (18), $\mathcal{H}[\tilde{y}_\alpha] - \mathcal{G}[\tilde{y}]$ in (31) can be approximated as

$$\mathcal{H}[\tilde{y}_\alpha] - \mathcal{G}[\tilde{y}] \simeq \mathcal{H}[D_\alpha^{(\rho)}\tilde{y}] - \mathcal{G}[\tilde{y}] = \sum_{k=-N/2}^{N/2-1} |k|(\rho(k) - 1)\,\hat{\tilde{y}}_k(t)\mathrm{e}^{\mathrm{i}k\alpha} \ . \tag{33}$$

Then the linearized equations in (31) yield the ordinary differential equations for the Fourier coefficients $\hat{\tilde{y}}_k$ and $\hat{\tilde{\phi}}_k$ of $\tilde{y}$ and $\tilde{\phi}$, respectively, as

$$\frac{\mathrm{d}}{\mathrm{d}t}\begin{pmatrix} \hat{\tilde{y}}_k \\ \hat{\tilde{\phi}}_k \end{pmatrix} = A \begin{pmatrix} \hat{\tilde{y}}_k \\ \hat{\tilde{\phi}}_k \end{pmatrix} \ , \tag{34}$$

with

$$A = \begin{pmatrix} -\dfrac{1}{2}k^2\rho(\rho-1) & |k|\rho \\ -\left(\dfrac{1}{2\pi {F_\lambda}^2} + \dfrac{2\pi}{W_e}k^2\rho^2\right) & 0 \end{pmatrix} \ . \tag{35}$$

The exponential growth rates of this linear system are given the eigenvalues ν's of A, namely

$$\nu_\pm = \frac{1}{4}k^2\rho(1-\rho) \pm \sqrt{\left\{\frac{1}{4}k^2\rho(1-\rho)\right\}^2 - \left(\frac{1}{2\pi {F_\lambda}^2} + \frac{2\pi}{W_e}k^2\rho^2\right)|k|\rho} \ . \tag{36}$$

Thus, unless $\rho = 0$ or 1, this scheme is linearly unstable. This result is the same as that in [4,5]. As noticed before, without any filtering function, or $\rho(k) = 1$, the scheme is neutrally stable.

To eliminate this instability associated with the use of filtering for spatial derivatives, Beale et al. [4,5] pointed out that the compatibility constraint

$$\mathcal{H}[\tilde{y}_\alpha] - \mathcal{G}[\tilde{y}] = 0 \ , \tag{37}$$

is required in the discretized form. In fact, if we apply the same filtering function $\rho(k)$ to $\tilde{y}$ as

$$\tilde{y}(\alpha, t) \simeq \sum_{k=-N/2}^{N/2-1} \rho(k)\hat{\tilde{y}}_k(t)\mathrm{e}^{\mathrm{i}k\alpha} =: \tilde{y}^{(\rho)}(\alpha, t) \ , \tag{38}$$

then $\mathcal{H}[\tilde{y}_\alpha] - \mathcal{G}[\tilde{y}]$ in (31) can be approximated as

$$\mathcal{H}[\tilde{y}_\alpha] - \mathcal{G}[\tilde{y}] \simeq \mathcal{H}[D_\alpha^{(\rho)}\tilde{y}] - \mathcal{G}[\tilde{y}^{(\rho)}] = 0 \ . \tag{39}$$

Namely the compatibility condition (37) is satisfied and the MEL method becomes linearly stable. Following this idea, when the singular integral in the double layer representation is evaluated, $z = z(\alpha, t)$ in the cotangent function of the singular integral is filtered in the MEL method, as shown in section 5.1. Note that Beale et al. [4,5] proved nonlinear stability of their scheme satisfying the compatibility condition (37).

4.2. The UHT method

In the Λ-plane, $y(\sigma,t)=0$ and $w=f_\sigma/z_\sigma=1$ in the equilibrium state on the free surface parametrized by $\Lambda=\mathrm{e}^{\mathrm{i}\sigma}$. Then the perturbed solutions z and f around the equilibrium can be expressed as

$$z(\sigma,t)=-\sigma+\tilde{z}(\sigma,t) \quad \text{and} \quad f(\sigma,t)=-\sigma+\tilde{f}(\sigma,t) \tag{40}$$

with $\tilde{z}(\sigma,t)$ and $\tilde{f}(\sigma,t)$ are the perturbed quantities of $O(\epsilon)$. Substituting these into the free surface conditions (9) and (10) and neglecting the high-order terms, we obtain the following linearized equations:

$$\begin{cases} \dfrac{\partial \tilde{y}}{\partial t} = \mathcal{H}[\tilde{\phi}_\sigma] \ , \\[2mm] \dfrac{\partial \tilde{\phi}}{\partial t} = 2\tilde{\phi}_\sigma + 2\mathcal{H}[\tilde{y}_\sigma] - \dfrac{1}{2\pi {F_\lambda}^2}\tilde{y} + \dfrac{2\pi}{W_e}\tilde{y}_{\sigma\sigma} \ . \end{cases} \tag{41}$$

Similarly to the case of MEL, we approximate $\tilde{y}$ and $\tilde{\phi}$ as (13) and their spatial derivatives using $D_\sigma^{(\rho)}$ in (18). Then the linearized equations in (41) produce the ordinary differential equations for the Fourier coefficients $\hat{\tilde{y}}_k$ and $\hat{\tilde{\phi}}_k$ of $\tilde{y}$ and $\tilde{\phi}$ as

$$\frac{\mathrm{d}}{\mathrm{d}t}\begin{pmatrix} \hat{\tilde{y}}_k \\ \hat{\tilde{\phi}}_k \end{pmatrix} = B \begin{pmatrix} \hat{\tilde{y}}_k \\ \hat{\tilde{\phi}}_k \end{pmatrix} \ , \tag{42}$$

with

$$B = \begin{pmatrix} 0 & |k|\rho \\ |k|\rho - \dfrac{1}{2\pi {F_\lambda}^2} - \dfrac{2\pi}{W_e}k^2\rho^2 & \mathrm{i}2k\rho \end{pmatrix} \ . \tag{43}$$

The eigenvalues ν of B are given by

$$\nu_\pm = \mathrm{i}k\rho \pm \mathrm{i}\sqrt{\left(\frac{1}{2\pi {F_\lambda}^2} + \frac{2\pi}{W_e}k^2\rho^2\right)|k|\rho} \ . \tag{44}$$

Since both $\nu_\pm$ in (44) do not have a positive real part, this scheme is linearly stable even when the filtering function $\rho(k)$ is applied only to spatial derivatives. This numerical stability is one of advantages of UHT over MEL.

It should be remarked that $\mathcal{G}[\tilde{y}]$ in (29) is the source of numerical instability of MEL, but no such terms appear in the linear stability analysis of UHT. This results from the difference of the cotangent function in the singular integrals in the two methods, as indicated at the end of section 3.2. This difference is directly related to the fact that the free surface, namely the boundary of the domain, moves with time in MEL, but not in the conformally mapped Λ-plane in UHT.

5. Numerical methods

This section summarizes the two numerical methods, MEL and UHT, which will be used for numerical comparison of the two methods in section 6. In both methods, we adopt (i) the Runge–Kutta method of 4th order for numerical integration and (ii) the pseudo-spectral method with FFT for numerical determination of the Fourier coefficients. For simplicity, we write each variable at $\alpha=\alpha_j$ or $\sigma=\sigma_j$ as

$$z(\alpha_j,t)=z_j(t) \ , \quad z(\sigma_j,t)=z_j(t) \ , \quad z_\alpha(\alpha_j,t)=z_{\alpha,j}(t) \quad \text{and} \quad z_\sigma(\sigma_j,t)=z_{\sigma,j}(t) \ . \tag{45}$$

5.1. The MEL method

Beale et al. [4] proposed the following approximations of the kinematic condition (7), the dynamic condition (8) and f_α in (5) with taking care of the compatibility constraint (37):

$$\frac{\mathrm{d}\bar{z}_j}{\mathrm{d}t}(t) = 1 + \frac{\gamma_j(t)}{2D_\alpha^{(\rho)}z_j(t)} + \frac{1}{4\pi\mathrm{i}}\sum_{\substack{k=0 \\ (k-j)\mathrm{odd}}}^{N-1} \gamma_k(t)\cot\left(\frac{z_j^{(\rho)}(t)-z_k^{(\rho)}(t)}{2}\right)\cdot 2\Delta\alpha \ , \tag{46}$$

$$\begin{aligned} \frac{\mathrm{d}\phi_j}{\mathrm{d}t}(t) &= \frac{1}{2}\{u_j(t)^2+v_j(t)^2\} + \frac{1}{2} - \frac{1}{2\pi {F_\lambda}^2}y_j(t) \\ &\quad + \frac{2\pi}{W_e}\frac{{D_\alpha^{(\rho)}}^2 y_j(t)\cdot D_\alpha^{(\rho)}x_j^{(p)}(t) - {D_\alpha^{(\rho)}}^2 x_j(t)\cdot D_\alpha^{(\rho)}y_j^{(p)}(t)}{\{(D_\alpha^{(\rho)}x_j^{(p)}(t))^2+(D_\alpha^{(\rho)}y_j^{(p)}(t))^2\}^{3/2}} \ , \end{aligned} \tag{47}$$

and

$$D_\alpha^{(\rho)} f_j(t) = D_\alpha^{(\rho)} z_j(t) + \frac{\gamma_j(t)}{2} + \frac{D_\alpha^{(\rho)} z_j(t)}{4\pi \mathrm{i}} \sum_{\substack{k=0 \\ (k-j)\mathrm{odd}}}^{N-1} \gamma_k(t) \cot\left(\frac{z_j^{(\rho)}(t) - z_k^{(\rho)}(t)}{2}\right) \cdot 2\Delta\alpha \ , \tag{48}$$

with

$$\gamma_j(t) = \gamma(\alpha_j, t) = \mu_\alpha(\alpha_j, t) \ . \tag{49}$$

The Fourier coefficients $\hat{z}_k(t)$ and $\hat{f}_k(t)$ are given by

$$\begin{cases} z_j(t) = t + \alpha_j + \displaystyle\sum_{k=-N/2}^{N/2-1} \hat{z}_k(t) \mathrm{e}^{\mathrm{i}k\alpha_j} \ , \\ f_j(t) = z_j(t) + \displaystyle\sum_{k=-N/2}^{N/2-1} \hat{f}_k(t) \mathrm{e}^{\mathrm{i}k\alpha_j} \ . \end{cases} \tag{50}$$

Note that, for the compatibility constraint (37), $z_j(t)$'s in the cotangent function of (46) and (48) are spectrally approximated by $z_j^{(\rho)}(t)$ with filtering as

$$z_j(t) \simeq z_j^{(\rho)}(t) = t + \alpha_j + \sum_{k=-N/2}^{N/2-1} \rho(k) \hat{z}_k(t) \mathrm{e}^{\mathrm{i}k\alpha_j} \ , \tag{51}$$

and, for balancing the high-mode error due to the nonlinearity of the surface tension term (see [4, p. 1819] or [25, p. 381]), $x_j(t)$'s and $y_j(t)$'s in the last term of (47) are approximated by $x_j^{(p)}(t)$ and $y_j^{(p)}(t)$, respectively, as

$$x_j(t) + \mathrm{i} y_j(t) \sim x_j^{(p)}(t) + \mathrm{i} y_j^{(p)}(t) = z_j^{(p)}(t) = t + \alpha_j + \sum_{k=-N/2}^{N/2-1} p(k) \hat{z}_k(t) \mathrm{e}^{\mathrm{i}k\alpha_j} \ , \tag{52}$$

with

$$p(k) = \frac{\mathrm{d}}{\mathrm{d}k}\{k\rho(k)\} = \rho(k) + k\frac{\mathrm{d}\rho}{\mathrm{d}k} \ . \tag{53}$$

Also $\gamma_j(t)$ can be numerically determined from (48) using an iterative scheme given by

$$\gamma_j^{(\nu+1)}(t) = 2D_\alpha^{(\rho)}\{\phi_j(t) - x_j(t)\} - \mathrm{Re}\left\{ \frac{D_\alpha^{(\rho)} z_j(t)}{2\pi \mathrm{i}} \sum_{\substack{k=0 \\ (k-j)\mathrm{odd}}}^{N-1} \gamma_k^{(\nu)}(t) \cot\left(\frac{z_j^{(\rho)}(t) - z_k^{(\rho)}(t)}{2}\right) \cdot 2\Delta\alpha \right\} \qquad (\nu = 0, 1, \cdots) \ , \tag{54}$$

where ν denotes the number of iterations. For the filtering function $\rho(k)$ in the spectral approximations in (18) and (51), we adopt the following two functions:

$$\rho_1(k) = \exp\{-10(2k/N)^{25}\} \ , \tag{55}$$

or

$$\rho_2(k) = \begin{cases} 1 & (0 \le |k| \le \frac{2}{3} \cdot \frac{N}{2}) \\ 0 & (\frac{2}{3} \cdot \frac{N}{2} < |k| \le \frac{N}{2}) \end{cases} \ . \tag{56}$$

As pointed out by Baker & Xie [3], the numerical error of MEL is sometimes sensitive to the choice of the filtering function, and it is difficult to find the optimum one. In this work, we tried some candidate functions which have been used in the previous works, and finally selected the above two functions which produce more accurate solutions. The smooth filter

$\rho_1(k)$ in (55) was introduced in [4, p. 1830] and the all-or-nothing filter such as $\rho_2(k)$ is often used in spectral methods [6, §11.5] [7, §3.2.2]. Note that ρ_2 does not satisfy the smoothness $\rho \in C^2$ assumed in [4, p. 1800] and $p(k)$ in (52) is set as $p(k) = \rho_2(k)$ for $\rho = \rho_2$, instead of (53).

The algorithm of MEL is summarized at the end of section 2.1.

5.2. The UHT method

For approximation of z and f in the Λ-plane, we can utilize analyticity of $\partial z/\partial f = \partial z/\partial \Lambda \cdot (\partial f/\partial \Lambda)^{-1}$ on the unit disk $|\Lambda| < 1$. Note that, without waves, $\partial z/\partial f(\Lambda, t) = 1$ and $f(\Lambda, t) = \mathrm{i}\log\Lambda$. Then we assume that $z(\Lambda, t)$ and $f(\Lambda, t)$ can be approximated by the truncated series expansion as

$$\begin{cases} z(\Lambda, t) \simeq \mathrm{i}\log\Lambda + \displaystyle\sum_{k=0}^{N/2} \{a_k(t) + \mathrm{i}b_k(t)\}\Lambda^k \ , \\ f(\Lambda, t) \simeq \mathrm{i}\log\Lambda + \displaystyle\sum_{k=0}^{N/2} \{c_k(t) + \mathrm{i}d_k(t)\}\Lambda^k \ , \end{cases} \tag{57}$$

where $a_k(t)$, $b_k(t)$, $c_k(t)$, and $d_k(t)$ are all real. At $\sigma = \sigma_j$ on the free surface $\Lambda = \mathrm{e}^{\mathrm{i}\sigma}$, the above approximation (57) yields

$$\begin{cases} y_j(t) = y(\alpha_j, t) \simeq \displaystyle\sum_{k=0}^{N/2} \{a_k(t)\sin k\sigma_j + b_k(t)\cos k\sigma_j\} \ , \\ \phi_j(t) = \phi(\alpha_j, t) \simeq -\sigma_j + \displaystyle\sum_{k=0}^{N/2} \{c_k(t)\cos k\sigma_j - d_k(t)\sin k\sigma_j\} \ , \end{cases} \tag{58}$$

and their spectral derivatives are given by

$$\begin{cases} y_{\sigma,j}(t) \simeq D_\sigma y_j(t) = \displaystyle\sum_{k=1}^{N/2} k\{a_k(t)\cos k\sigma_j - b_k(t)\sin k\sigma_j\} \ , \\ \phi_{\sigma,j}(t) \simeq D_\sigma \phi_j(t) = -1 - \displaystyle\sum_{k=1}^{N/2} k\{c_k(t)\sin k\sigma_j + d_k(t)\cos k\sigma_j\} \ . \end{cases} \tag{59}$$

We can numerically determine the real coefficients $a_k(t)$, $b_k(t)$, $c_k(t)$, and $d_k(t)$ from $y_j(t)$ and $\phi_j(t)$ using FFT.

From these, the surface Euler equations (9) and (10) can be evaluated at $\sigma = \sigma_j$ and approximated, respectively, as

$$\frac{\mathrm{d}y_j}{\mathrm{d}t} = -D_\sigma x_j \cdot \frac{1}{(D_\sigma s_j)^2} D_\sigma \psi_j + D_\sigma y_j \cdot \mathcal{H}\left[\frac{1}{(D_\sigma s_j)^2} D_\sigma \psi_j\right] \ , \tag{60}$$

and

$$\begin{aligned} \frac{\mathrm{d}\phi_j}{\mathrm{d}t} &= D_\sigma \phi_j \cdot \mathcal{H}\left[\frac{1}{(D_\sigma s_j)^2} D_\sigma \psi_j\right] - \frac{1}{2(D_\sigma s_j)^2}\{(D_\sigma \phi_j)^2 - (D_\sigma \psi_j)^2\} \\ &\quad + \frac{1}{2} - \frac{1}{2\pi F_\lambda{}^2} y_j - \frac{2\pi}{W_e} \frac{D_\sigma{}^2 y_j \cdot D_\sigma x_j - D_\sigma{}^2 x_j \cdot D_\sigma y_j}{(D_\sigma s_j)^3} \ , \end{aligned} \tag{61}$$

where

$$D_\sigma s_j = \sqrt{(D_\sigma x_j)^2 + (D_\sigma y_j)^2} \ . \tag{62}$$

Here we can obtain $\mathcal{H}[D_\sigma \psi_j/(D_\sigma s_j)^2]$ using (21), and determine $D_\sigma x_j(t)$ and $D_\sigma \psi_j(t)$ using $x_j(t) = \mathrm{Re}\{z_j(t)\}$ and $\psi_j(t) = \mathrm{Im}\{f_j(t)\}$ with (57) and the coefficients $a_k(t)$, $b_k(t)$, $c_k(t)$, and $d_k(t)$ obtained from $y_j(t)$ and $\phi_j(t)$ in (58) as

$$\begin{cases} D_\sigma x_j(t) = -1 - \displaystyle\sum_{k=1}^{N/2} k\{a_k(t)\sin k\sigma_j + b_k(t)\cos k\sigma_j\} \ , \\ D_\sigma \psi_j(t) = \displaystyle\sum_{k=1}^{N/2} k\{c_k(t)\cos k\sigma_j - d_k(t)\sin k\sigma_j\} \ . \end{cases} \tag{63}$$

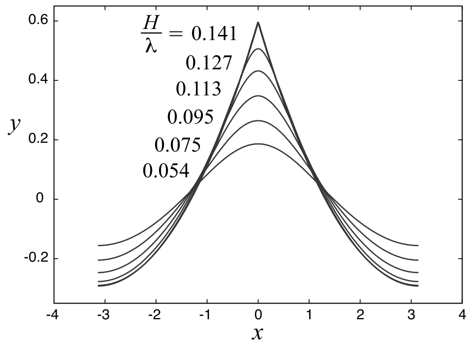

Fig. 2. Wave profiles of pure gravity waves progressing in permanent form for different values of the wave height-to-length ratio H/λ. Wave profiles are computed using Yamada's method [51,35].

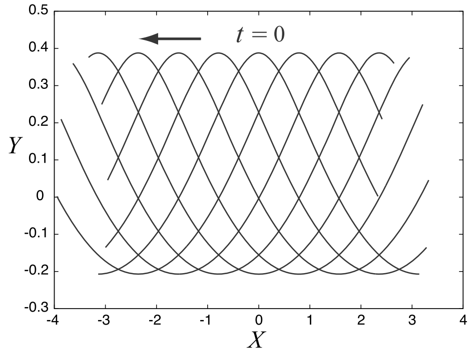

Fig. 3. Time evolution of wave profiles of pure gravity waves progressing to the left in the inertial frame. Time interval of each wave profile is $2\pi/8$. The initial value is the steady solution of pure gravity waves progressing in permanent form with $H/\lambda = 0.095$ ($F_\lambda = 0.4170$). The numerical method is MEL with $F_\lambda = 0.4170$, $1/W_e = 0$, $N = 256$, $\Delta t = 2\pi/2048$ and filtering (55).

Note that the filtering technique was not required for numerical computation using UHT in section 6. The algorithm of UHT is summarized at the end of section 2.2.

6. Numerical comparison of the two methods

In this section, we compare the two methods, MEL and UHT, using some computed results for the three cases: (i) pure gravity waves progressing in permanent form, (ii) pure capillary waves progressing in permanent form, and (iii) parasitic capillary waves. All of the computed results were obtained using the numerical methods described in section 5. To estimate the accuracy of the computed results, we monitor an error index $E_{\rm error}(t)$ defined by

$$E_{\rm error}(t) = \frac{|E_{\rm T}(t) - E_{\rm T}(0)|}{E_{\rm T}(0)} \quad \text{with } E_{\rm T}(t) = E_{\rm K}(t) + E_{\rm P}(t) + E_{\rm S}(t) \ , \tag{64}$$

where $E_{\rm T}(t)$ denotes the total energy of waves, namely the sum of the kinetic energy $E_{\rm K}(t)$, the potential energy $E_{\rm P}(t)$, and the surface energy $E_{\rm S}(t)$. From the energy conservation law, this index $E_{\rm error}(t)$ always vanishes for exact solutions. See Appendix for computation of each energy. Note that N denotes the number of truncated Fourier series for spectral approximation, and Δt is the time increment of the Runge–Kutta method of 4th order for numerical integration. Also, in MEL, the filtering function $\rho_1(k)$ in (55) is used for (i) pure gravity waves and (ii) pure capillary waves, and $\rho_2(k)$ in (56) is for (iii) parasitic capillary waves. It is because, for the case of (iii), MEL with ρ_2 is numerically more stable than that with ρ_1 under the conditions of numerical examples in this section.

6.1. Pure gravity waves progressing in permanent form

We can obtain numerically highly accurate solutions of fully nonlinear motion of pure gravity waves progressing in permanent form on water of infinite depth, assuming that the flow is steady in the moving frame [41,49]. Fig. 2 shows some computed steady wave profiles for different values of the wave height-to-length ratio H/λ, which are obtained using Yamada's method [51,35]. We used these steady solutions as initial conditions for the two numerical methods described in section 5. As an example, in the absence surface tension ($1/W_e = 0$), Fig. 3 shows the computed result using MEL for the propagation of a pure gravity wave of $F_\lambda = 0.4170$ ($H/\lambda = 0.095$).

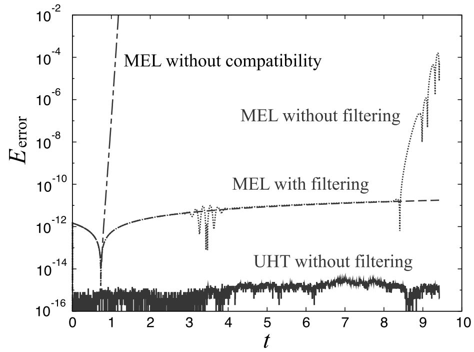

Fig. 4. Comparison of the error index $E_{\rm error}(t)$ of MEL and UHT for pure gravity waves progressing in permanent form with $H/\lambda = 0.095$ ($F_\lambda = 0.4170$). The error index is defined by (64). The computational conditions are $F_\lambda = 0.4170$, $1/W_e = 0$, $N = 256$ and $\Delta t = 2\pi/2048$. Solid line: UHT without filtering, dashed line: MEL with filtering (55), dotted line: MEL without filtering, and dot-dashed line: MEL without compatibility condition (37).

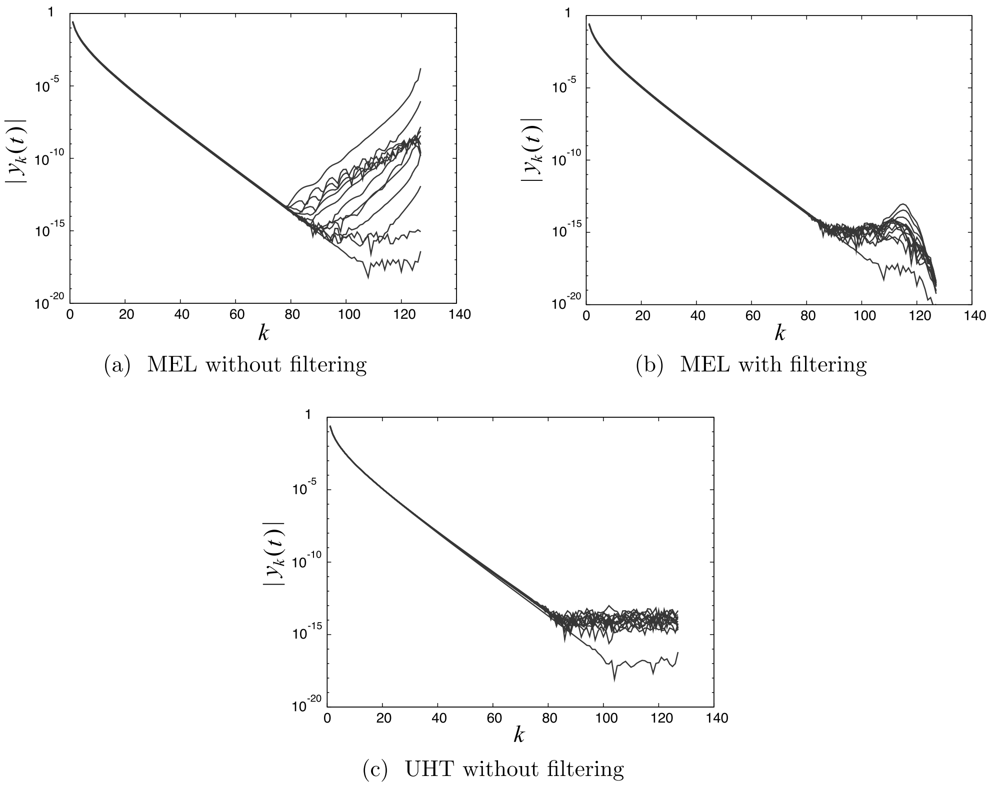

Fig. 5. Time variation of the absolute value $|\hat{y}_k(t)|$ of the Fourier coefficients of $y(\alpha, t)$ in MEL and $y(\sigma, t)$ in UHT for pure gravity waves progressing in permanent form with $H/\lambda = 0.095$ ($F_\lambda = 0.4170$). Each line shows the result at different time $t = j \times 2\pi/16$ ($j = 0, 2, \cdots, 24$). The computational conditions are $F_\lambda = 0.4170$, $1/W_e = 0$, $N = 256$ and $\Delta t = 2\pi/2048$. (a) MEL without filtering, (b) MEL with filtering (55), and (c) UHT without filtering.

Fig. 4 shows time variation of the error index $E_{\rm error}(t)$ in (64) of the two methods for pure gravity waves with $F_\lambda = 0.4170$ ($H/\lambda = 0.095$). The results demonstrate that MEL requires both the compatibility condition (37) and the filtering technique (18) with $\rho = \rho_1$ in (55) for stable and accurate computation, while UHT is stable and produces highly accurate solutions even without filtering.

Fig. 5 compares the time variation of the absolute value $|\hat{y}_k(t)|$ of the Fourier coefficients of $y(\alpha, t)$ in MEL or $y(\sigma, t)$ in UHT for the three cases: MEL with and without filtering and UHT without filtering. We can see that the filtering technique in MEL is required to control high wave number modes while no such techniques are needed for UHT.

6.2. Pure capillary waves progressing in permanent form

Crapper [15] obtained an exact solution for pure capillary waves progressing in permanent form, which can be represented in UHT by

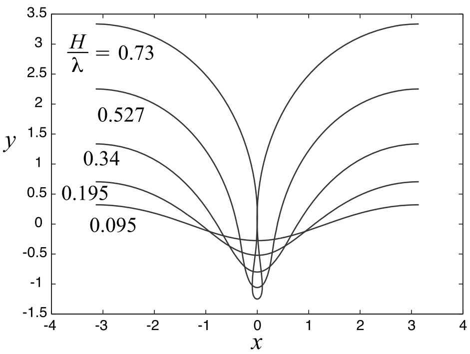

Fig. 6. Wave profiles of pure capillary waves progressing in permanent form for different values of the wave height-to-length ratio H/λ. Wave profiles are computed using Crapper's solution (65).

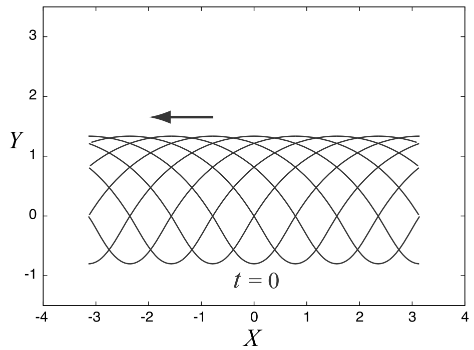

Fig. 7. Time evolution of wave profiles of pure capillary waves progressing to the left in the inertial frame. Time interval of each wave profile is $2\pi/8$. The initial value is Crapper's solution (65) for $H/\lambda = 0.34$. The numerical method is UHT with $1/F_\lambda = 0$, $1/W_e = 0.1804$, $N = 256$ and $\Delta t = 2\pi/16384$ and without filtering.

$$\begin{cases} x(\sigma) = -\sigma + 4\dfrac{A\sin\sigma}{1 + A^2 + 2A\cos\sigma}\,, \\ y(\sigma) = -4\left(1 - \dfrac{1 + A\cos\sigma}{1 + A^2 + 2A\cos\sigma}\right)\,, \end{cases} \tag{65}$$

where

$$A = \left(\frac{2\pi}{W_e} - 1\right) \Bigg/ \sqrt{\left(\frac{2\pi}{W_e}\right)^2 - 1}\,, \tag{66}$$

and the wave height-to-length ratio H/λ is given by

$$\frac{H}{\lambda} = \frac{2}{\pi}\sqrt{\left(\frac{2\pi}{W_e}\right)^2 - 1}\,. \tag{67}$$

Note that, by changing σ to $-\alpha$ in (65), the corresponding solution for MEL can be obtained.

Fig. 6 shows wave profiles with different values of H/λ obtained using Crapper's exact solution (65), which are used as initial conditions for the numerical methods without gravity ($1/F_\lambda = 0$) described in section 5. Fig. 7 shows that, even without filtering, UHT produces an accurate numerical solution for the propagation of a pure capillary wave train of $H/\lambda = 0.34$, as demonstrated in Fig. 8, where the variation of the error index $E_{\text{error}}(t)$ is shown. However, the numerical computation using MEL became unstable and its error index $E_{\text{error}}(t)$ diverged even for small amplitude waves with small time increment Δt and the filtering function $\rho = \rho_1$ in (55), as shown in Fig. 8. These results suggest that UHT is more suitable for computation of pure capillary waves. In section 7, we will discuss this difference between the two methods from the point of view of spatial resolution on the free surface.

6.3. Parasitic capillary waves

For numerical computation of parasitic capillary waves for $F_\lambda = F_\lambda^*$ and $1/W_e > 0$, we used the steady solution of pure gravity waves for $F_\lambda = F_\lambda^*$ and $1/W_e = 0$ as the initial condition of the two numerical methods. Fig. 9 compares the time

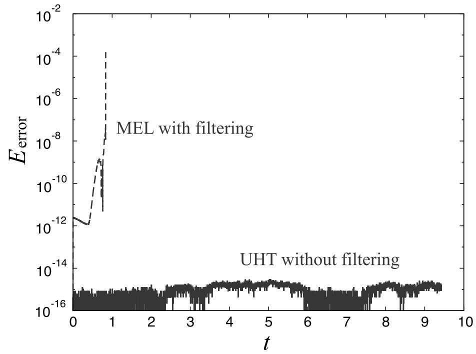

Fig. 8. Comparison of the error index $E_{\rm error}(t)$ of MEL and UHT for pure capillary waves progressing in permanent form with $H/\lambda = 0.34$ $(1/W_e = 0.1804)$. The error index is defined by (64). The computational conditions are $1/F_\lambda = 0$, $1/W_e = 0.1804$, $N = 256$, $\Delta t = 2\pi/65536$ (MEL) and $\Delta t = 2\pi/16384$ (UHT). Dashed line: MEL with filtering (55) and solid line: UHT without filtering.

evolution of the wave slope defined by $\theta = \arctan(\partial y/\partial x)$ and the wave profile in the frame of reference moving with waves for $F_\lambda = 0.4170$ and $1/W_e = 0.006$. The dashed and solid lines in these figures show the computed results using MEL and UHT, respectively. Notice that the wave slope θ can be computed from $\theta = \arctan(y_\alpha/x_\alpha)$ in MEL, or $\theta = \arctan(y_\sigma/x_\sigma)$ in UHT. Also note that, in MEL, the filtering function $\rho_2(k)$ in (56) is used because it is numerically more stable than $\rho_1(k)$ in (55) for parasitic capillary waves under these conditions. These results show that both methods can describe the initial stage of generation of parasitic capillary waves on the forward face of left-going primary gravity waves, but MEL becomes numerically unstable after the generation of capillary waves, as shown in Fig. 9(f).

Fig. 10 compares the error index $E_{\rm error}(t)$ in (64) of the computed results obtained using the two methods, MEL and UHT. From the results in Figs. 9 and 10, it can be concluded that UHT, even without filtering, can be more accurate and stable than MEL with filtering. It was also found that the error index $E_{\rm error}(t)$ of MEL in Figs. 8 and 10 can be reduced by improving spatial and temporal resolutions, namely, increasing the number of modes of truncated Fourier series N or decreasing the time increment Δt, but finally grows with time after the generation of capillary waves. In section 7, we will give a possible explanation on this difference between the two methods.

Fig. 11 shows time variation of the wave energies $E_K(t)$, $E_P(t)$, $E_S(t)$, and $E_T(t)$, of the computed results in Fig. 9. We can see periodic change of $E_K(t)$ and $E_P(t)$ with almost the same period as the underlying gravity waves. This periodic behavior may be related to nonlinear recurrence observed in [19,28], although it is not so obvious in the time evolution of wave profile shown in Fig. 9.

7. Distribution of the sample points on the free surface

In both methods, the spatial coordinate along the free surface, namely α in MEL or σ in UHT, is discretized with an equal interval as α_j in (14) or σ_j in (15) $(j = 0, 1, \cdots, N)$, respectively, for numerical determination of the Fourier coefficients using FFT. Then it should be noted that, in the physical plane, the corresponding sample points $(x_j(t), y_j(t)) = (x(\alpha_j, t), y(\alpha_j, t))$ or $(x(\sigma_j, t), y(\sigma_j, t))$ on the free surface are not uniformly distributed. For accurate computation, it is desirable that the sample points (x_j, y_j) are clustered near the point at which the wave profile sharply changes, such as the crest of pure gravity waves in Fig. 2 or the trough of pure capillary waves in Fig. 6. Therefore we examine the distribution of the sample points on the free surface and its time variation to better understand the solution behaviors of the two different methods.

7.1. MEL for pure gravity waves and pure capillary waves

Figs. 12 and 13 compare the time variation of the sample point distribution on the free surface of pure gravity waves and pure capillary waves, respectively, when the MEL scheme is adopted. Fig. 12 enlarges the sample point distribution near the crest of pure gravity waves progressing to the left in permanent form with $H/\lambda = 0.095$ obtained in section 6.1. One can see that, in MEL, the sample points are clustered near the crest of gravity waves and the spatial resolution increases there with time. On the other hand, Fig. 13 enlarges the sample point distribution near the trough of pure capillary waves progressing to the left in permanent form with $H/\lambda = 0.34$ obtained in section 6.2. It is found that, in MEL, the sample points move fast away from the trough of capillary waves and the spatial resolution decreases there with time.

In the case of MEL, the velocity distribution on the free surface determines the sample point distribution as can be seen from the kinematic condition (7). For example, the sample point is stationary at the crest of the highest gravity wave, which corresponds to the stagnation point with $u = v = 0$. Thus, near the crest of gravity waves of large amplitude, the sample points move slowly and are clustered. Figs. 14 (a) and (b) show the distribution of $q = \sqrt{u^2 + v^2}$ on the free surface of pure gravity waves and pure capillary waves, respectively. We can see that the absolute velocity q is minimum at the crest $x = 0$

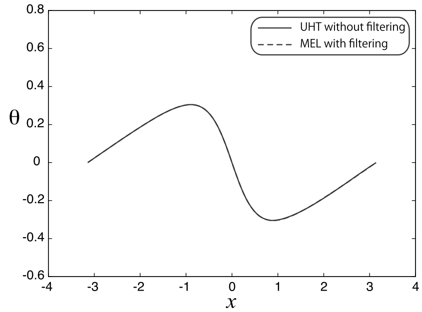

(a.1) Slope θ

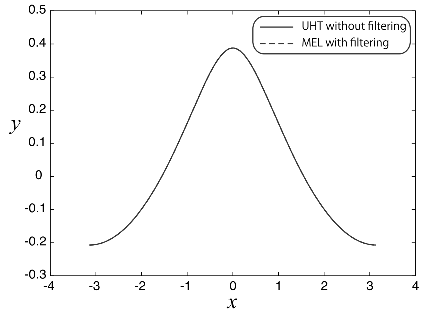

(a.2) Wave profile

(a) $t = 0$

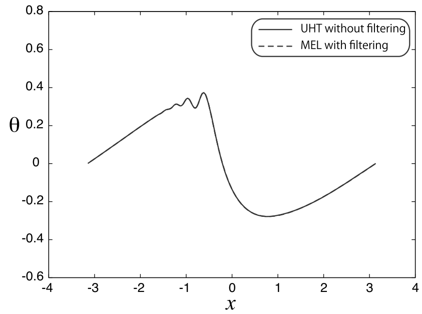

(b.1) Slope θ

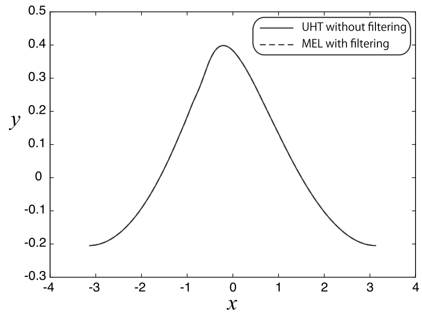

(b.2) Wave profile

(b) $t = 8 \times 2\pi/16$

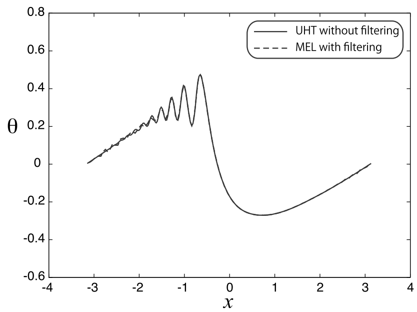

(c.1) Slope θ

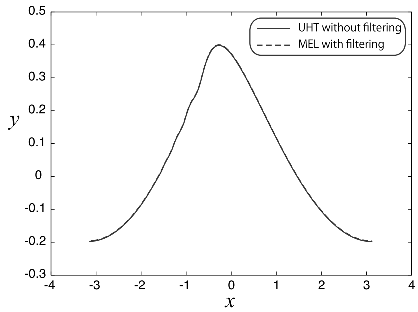

(c.2) Wave profile

(c) $t = 12 \times 2\pi/16$

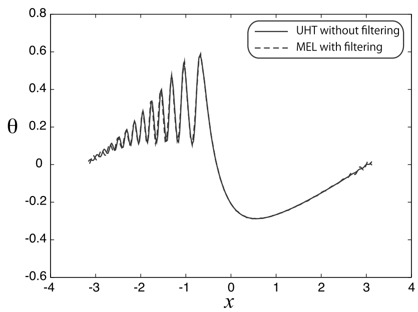

(d.1) Slope θ

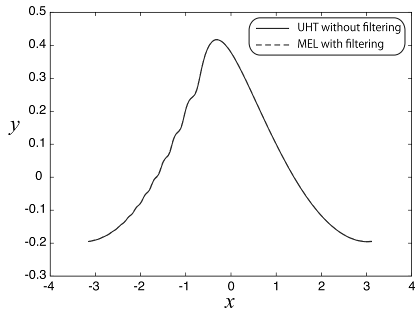

(d.2) Wave profile

(d) $t = 16 \times 2\pi/16$

Fig. 9. Time evolution of the slope θ on the free surface and the wave profile for gravity-capillary waves with $F_\lambda = 0.4170$ and $1/W_e = 0.006$. $\theta = \arctan(y_\alpha/x_\alpha)$ (MEL) and $\arctan(y_\sigma/x_\sigma)$ (UHT). Dashed line: MEL with filtering (56) and solid line: UHT without filtering. The initial value is the steady solution of pure gravity waves progressing in permanent form with $H/\lambda = 0.095$ ($F_\lambda = 0.4170$). The computational conditions are $N = 256$ and $\Delta t = 2\pi/2048$.

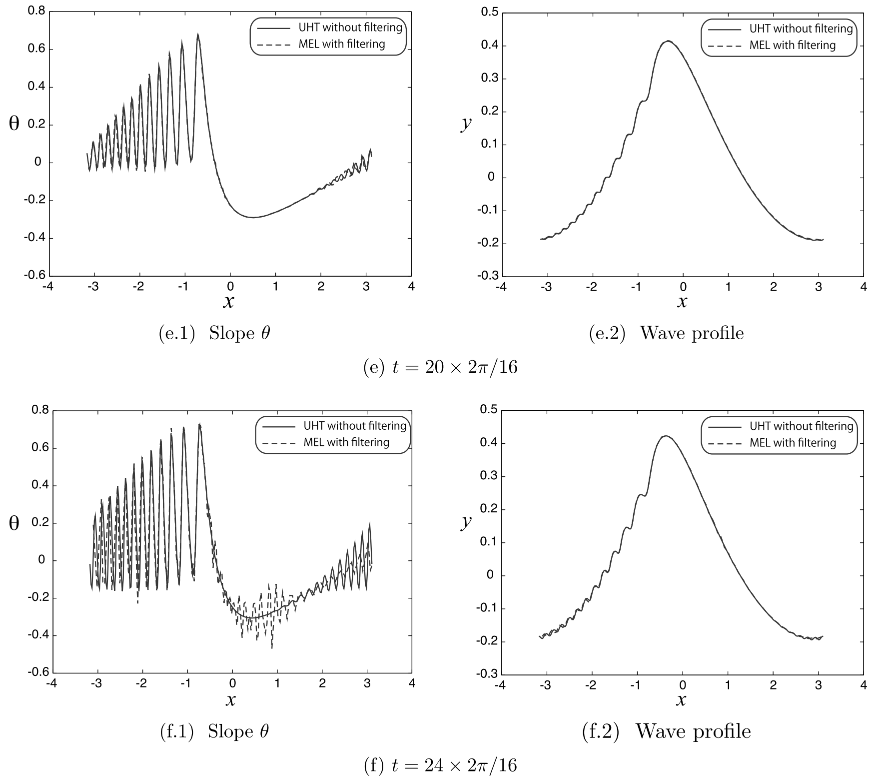

(e.1) Slope θ (e.2) Wave profile

(e) $t = 20 \times 2\pi/16$

(f.1) Slope θ (f.2) Wave profile

(f) $t = 24 \times 2\pi/16$

Fig. 9. (*continued*)

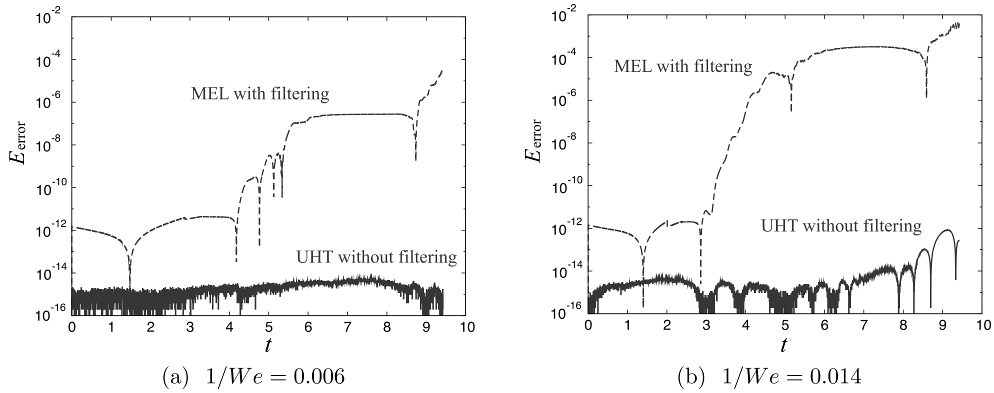

(a) $1/We = 0.006$ (b) $1/We = 0.014$

Fig. 10. Comparison of the error index $E_{\text{error}}(t)$ for gravity-capillary waves with $F_\lambda = 0.4170$. The error index is defined by (64). Dashed line: MEL with filtering (56) and solid line: UHT without filtering. The initial value is the steady solution of pure gravity waves progressing in permanent form with $H/\lambda = 0.095$ ($F_\lambda = 0.4170$). The computational conditions are (a) $F_\lambda = 0.4170$, $1/W_e = 0.006$, $N = 512$ and $\Delta t = 2\pi/4096$, and (b) $F_\lambda = 0.4170$, $1/W_e = 0.014$, $N = 256$ and $\Delta t = 2\pi/4096$.

of pure gravity waves, and maximum at the trough $x = 0$ of pure capillary waves. This elucidates the clustering property of sample points in MEL, which was observed in Figs. 12 and 13.

7.2. UHT for pure gravity waves and pure capillary waves

In the case of UHT, the distribution of sample points on the free surface is initially the same as that in MEL, but is almost unchanged with time for waves progressing in permanent form. The initial distribution depends on $s_\sigma = \sqrt{{x_\sigma}^2 + {y_\sigma}^2}$, and the points are clustered near the point at which s_σ is small. In the case of pure capillary waves progressing in permanent form, Crapper's exact solution (65) can be written in the form

$$\frac{dz}{df} = \left(\frac{1 - A\Lambda}{1 + A\Lambda}\right)^2 , \tag{68}$$

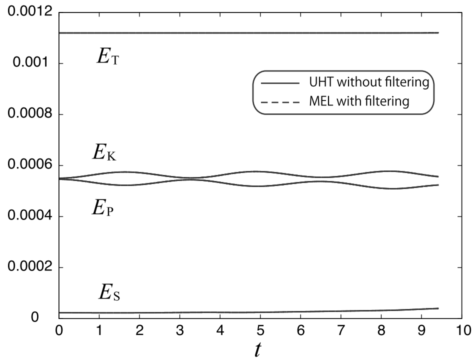

Fig. 11. Time evolution of the kinetic energy E_K, the potential energy E_P, the surface energy E_S and the total energy $E_\mathrm{T} = E_\mathrm{K} + E_\mathrm{P} + E_\mathrm{S}$ for gravity-capillary waves with $F_\lambda = 0.4170$ and $1/We = 0.006$. Dashed line: MEL with filtering (56) and solid line: UHT without filtering. The initial value is the steady solution of pure gravity waves progressing in permanent form with $H/\lambda = 0.095$ ($F_\lambda = 0.4170$). The computational conditions are $N = 256$ and $\Delta t = 2\pi/2048$.

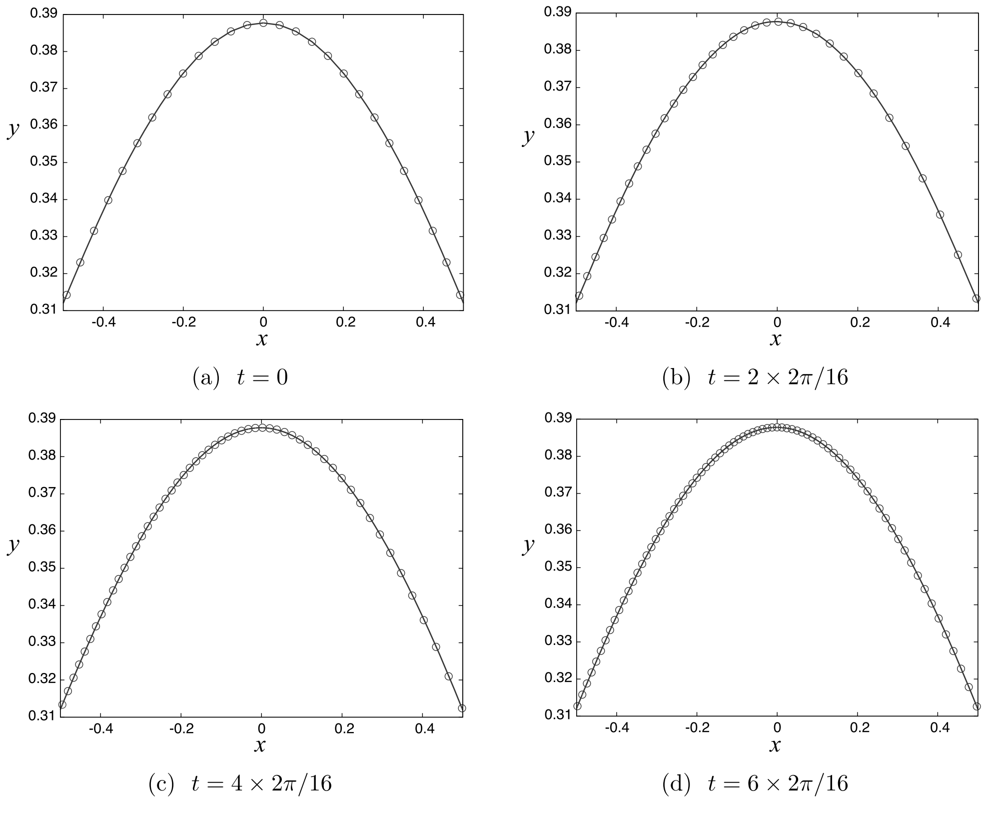

Fig. 12. Time evolution of the sample point distribution near the crest of pure gravity waves progressing in permanent form with $H/\lambda = 0.095$ ($F_\lambda = 0.4170$). The numerical method is MEL with $N = 256$, $\Delta t = 2\pi/2048$ and filtering (55).

and, from this, we can obtain $s_\sigma = |\mathrm{d}z/\mathrm{d}\sigma| = |\mathrm{d}z/\mathrm{d}f| \cdot |\mathrm{d}f/\mathrm{d}\sigma|$ as

$$s_\sigma = \left|\frac{1 - A\mathrm{e}^{\mathrm{i}\sigma}}{1 + A\mathrm{e}^{\mathrm{i}\sigma}}\right|^2 \to \begin{cases} \left(\dfrac{1-A}{1+A}\right)^2 < 1 & (\sigma \to 0\ : \text{trough}) \\ \left(\dfrac{1+A}{1-A}\right)^2 > 1 & (\sigma \to \pm\pi\ : \text{crest}) \end{cases}. \tag{69}$$

Therefore, one can expect that more sample points are clustered near the trough for pure capillary waves.

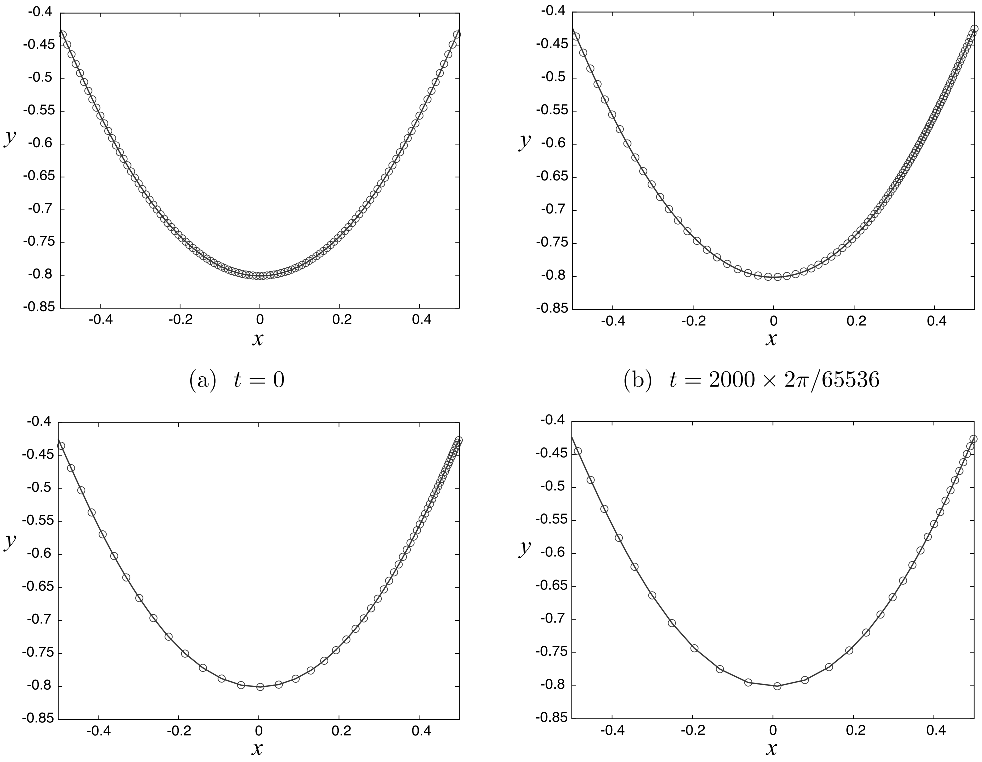

(a) $t = 0$ (b) $t = 2000 \times 2\pi/65536$

(c) $t = 4000 \times 2\pi/65536$ (d) $t = 6000 \times 2\pi/65536$

Fig. 13. Time evolution of the sample point distribution near the trough of pure capillary waves progressing in permanent form with $H/\lambda = 0.34$ ($1/W_e = 0.1804$). The numerical method is MEL with $N = 256$, $\Delta t = 2\pi/65536$ and filtering (55).

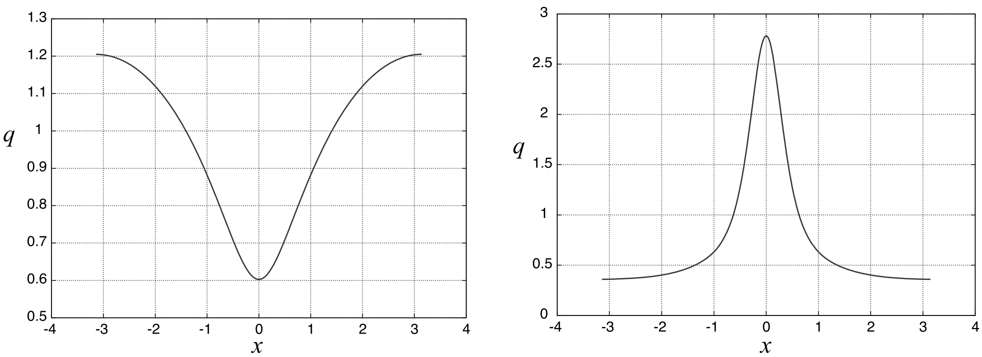

(a) Pure gravity wave ($H/\lambda = 0.095$) (b) Pure capillary wave ($H/\lambda = 0.34$)

Fig. 14. Distribution of the absolute value $q = \sqrt{u^2 + v^2}$ of velocity on the free surface of pure gravity waves with $H/\lambda = 0.095$ ($F_\lambda = 0.4170$) and pure capillary waves with $H/\lambda = 0.34$ ($1/W_e = 0.1804$) in the frame of reference moving with waves. These waves are progressing in permanent form. In (a), $x = 0$ and $x = \pm\pi$ correspond to the crest and the trough of pure gravity waves, respectively. In (b), $x = 0$ and $x = \pm\pi$ correspond to the trough and the crest of pure capillary waves, respectively.

For comparison, in the case of pure gravity waves progressing in permanent form, we can use Davies' approximate solution [16] given by

$$\frac{\mathrm{d}z}{\mathrm{d}f} = (1 - \beta\Lambda)^{-1/3} \quad \text{with } 0 \le \beta \le 1 \ , \tag{70}$$

from which s_σ can be found as

$$s_\sigma = \left|1 - \beta \mathrm{e}^{\mathrm{i}\sigma}\right|^{-1/3} \to \begin{cases} (1-\beta)^{-1/3} > 1 & (\sigma \to 0 \ : \text{crest}) \\ (1+\beta)^{-1/3} < 1 & (\sigma \to \pm\pi \ : \text{trough}) \end{cases} \ . \tag{71}$$

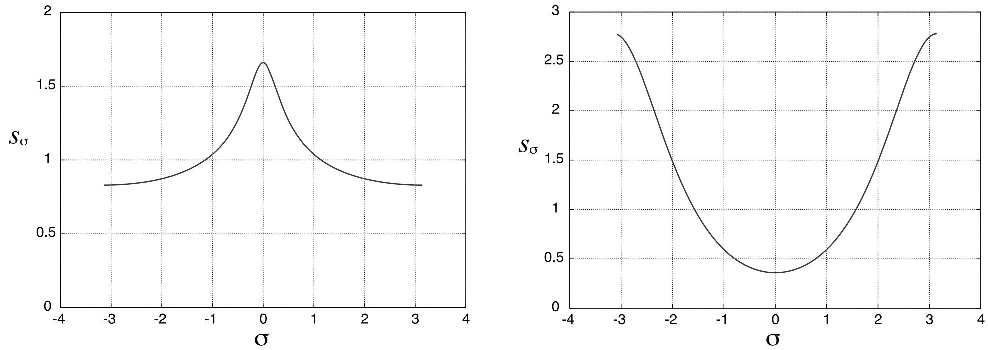

(a) Pure gravity wave ($H/\lambda = 0.095$) (b) Pure capillary wave ($H/\lambda = 0.34$)

Fig. 15. Distribution of $s_\sigma = \sqrt{x_\sigma{}^2 + y_\sigma{}^2}$ on the free surface of pure gravity waves with $H/\lambda = 0.095$ ($F_\lambda = 0.4170$) and pure capillary waves with $H/\lambda = 0.34$ ($1/W_e = 0.1804$). These waves are progressing in permanent form. In (a), $\sigma = 0$ and $\sigma = \pm\pi$ correspond to the crest and the trough of pure gravity waves, respectively. In (b), $\sigma = 0$ and $\sigma = \pm\pi$ correspond to the trough and the crest of pure capillary waves, respectively.

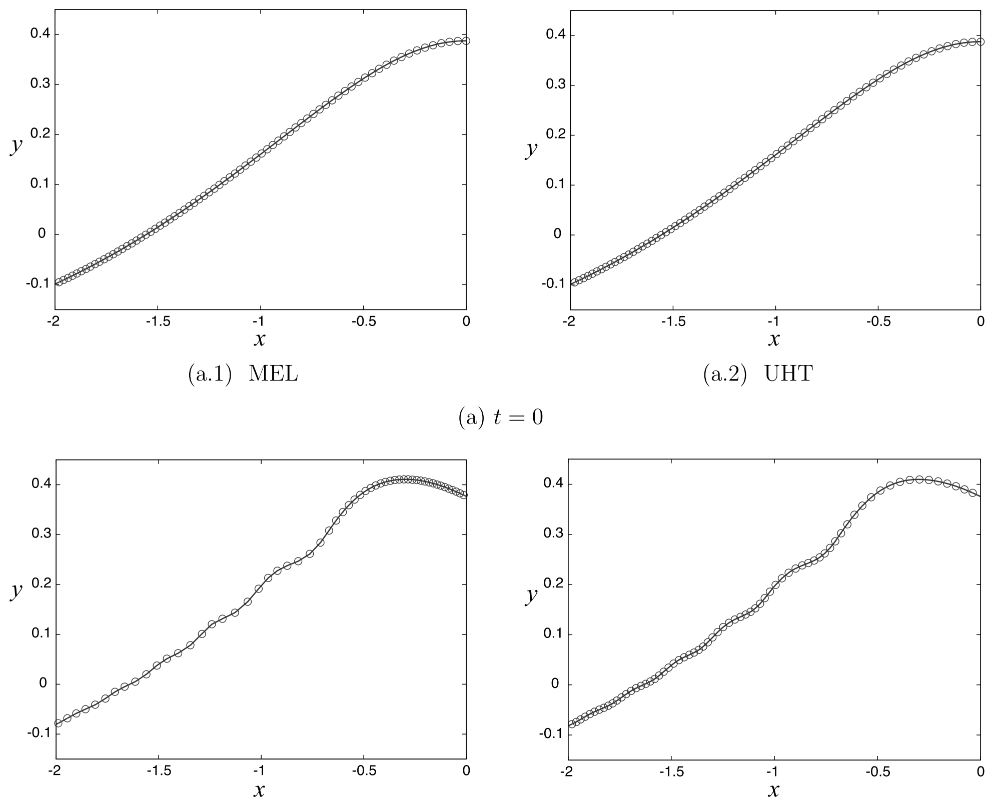

(a.1) MEL (a.2) UHT

(a) $t = 0$

(b.1) MEL (b.2) UHT

(b) $t = 14 \times 2\pi/16$

Fig. 16. Comparison of time evolution of the sample point distribution on the forward face ($-2 \le x \le 0$) near the crest of gravity-capillary waves with $F_\lambda = 0.4170$ and $1/W_e = 0.006$. Left: MEL with filtering (56), and right: UHT without filtering. The computational conditions are $N = 256$ and $\Delta t = 2\pi/2048$.

Under Davies' approximation, the wave steepness H/λ increases with β, and $\beta = 1$ corresponds to the highest wave that has a stagnation point at the crest with a corner whose inner angle is 120 degrees. From Figs. 15 (a) and (b) for the distribution of s_σ for pure gravity waves and pure capillary waves, respectively, one can conclude, along with eqs. (69) and (71), that the sample points are clustered near the trough of capillary waves at which s_σ is minimum, but not near the crest of gravity waves at which s_σ is maximum. Thus, when the UHT scheme is used, the free surface is well-resolved near the trough of capillary waves, but is poorly-resolved near the crest of gravity waves.

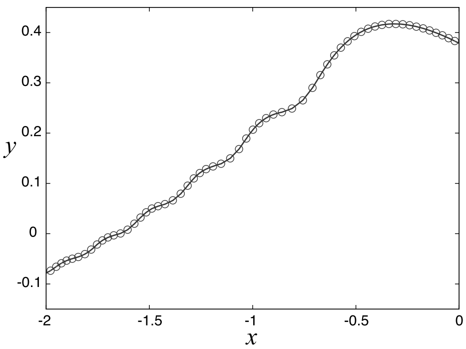

(c.1) MEL

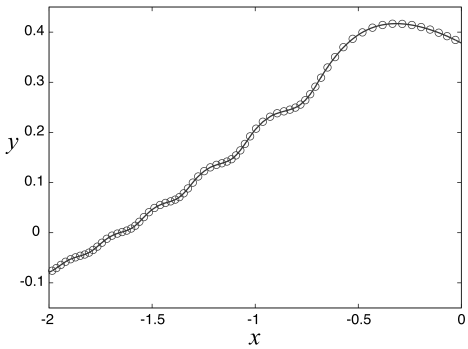

(c.2) UHT

(c) $t = 16 \times 2\pi/16$

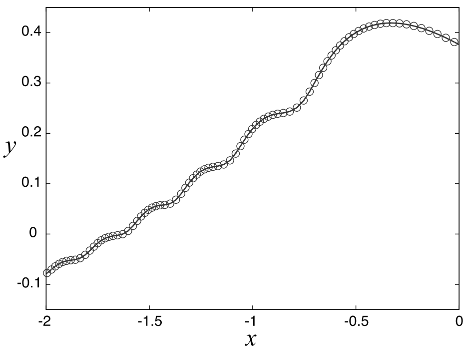

(d.1) MEL

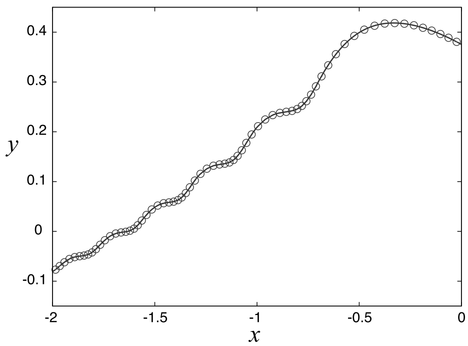

(d.2) UHT

(d) $t = 18 \times 2\pi/16$

Fig. 16. (*continued*)

7.3. MEL and UHT for parasitic capillary waves

Fig. 16 compares the time variation of the sample point distribution on the free surface for gravity-capillary waves with $F_\lambda = 0.4170$ and $1/W_e = 0.006$. The initial wave profile is the traveling gravity wave solution obtained in section 6.3. This figure enlarges the forward face near the crest of the underlying gravity wave. The results can be summarized as

(i) At the initial stages ($t \le 14 \times 2\pi/16$)
In MEL, the sample points are clustered near the crest ($-0.5 \le x \le 0$) of the underlying gravity wave, and the spatial resolution decreases for $x \le -0.7$ where parasitic capillary waves are generated, as shown in Fig. 16(b.1). On the other hand, in UHT, the spatial resolution for $x \le -0.7$ remains almost the same, as shown in Fig. 16(b.2).

(ii) After generation of parasitic capillary waves ($t > 14 \times 2\pi/16$)
In MEL, the sample points are clustered not only near the crest of the underlying gravity wave, but also near each crest of parasitic capillary waves, as shown in Figs. 16(c.1) and (d.1). On the other hand, in UHT, the sample points are clustered near each trough of parasitic capillary waves, as shown in Figs. 16(c.2) and (d.2).

These results demonstrate that UHT is advantageous over MEL for computation of parasitic capillary waves as the spatial resolution is required near the trough of capillary waves, as shown in Fig. 6 and described in section 7.2. On the other hand, as shown in Figs. 16(c.1) and (d.1) and described in section 7.1, the sample points on the free surface in MEL tend to cluster near the crest of waves, which is desirable for computation of steep gravity waves. These results indicate that, from the point of view of spatial resolution on the free surface, UHT is suitable for computation of capillary dominated waves, while MEL is for gravity dominated waves.

The sample points on the free surface could be redistributed such that they are always clustered near the point at which wave profile sharply changes (for example [2]). Nevertheless, application of this idea to UHT should be explored with care not to compromise numerical accuracy, which is left for a future work.

8. Conclusions

We have considered two different numerical methods for fully nonlinear computation of unsteady motion of gravity-capillary waves, with focusing on the formation of parasitic capillary waves on a traveling gravity wave, on water of infinite depth within the framework of irrotational plane flow. One is the Mixed-Eulerian–Lagrangian (MEL) method based on a boundary integral formulation presented in section 2.1, and the other is the method using unsteady conformal mapping, the unsteady hodograph transformation (UHT) method in section 2.2. In UHT, the flow domain is mapped onto the unit disk and the free surface is fixed on the unit circle, as shown in Fig. 1.

In both methods, spatial derivatives are spectrally estimated under periodic boundary conditions, as shown in section 3.1. To control aliasing errors due to the use of truncated Fourier series, a filtering function is applied when taking spatial derivatives. The linear stability analysis around the equilibrium in section 4 has shown that MEL is unstable only when a filtering function is used only for spatial derivatives and requires the additional condition (37) to ensure its stability [4,5]. On the other hand, UHT is shown linearly stable even when the same filtering function is applied only to spatial derivatives. This difference arises from the nature of singular integrals in the two methods. It should be remembered that the free surface is mapped onto a flat surface or a unit circle in UHT, but it is moving in time in MEL. As a consequence, the kernel of cotangent function in MEL depends on the dependent variable z, and, therefore, nonlinear while that in UHT is independent of any dependent variables.

We have presented some computed results using the two methods, MEL and UHT, for pure gravity waves, pure capillary waves, and gravity-capillary waves, in section 6. For both methods, a pseudo-spectral method based on FFT has been used to compute spatial derivatives, and the Runge–Kutta method of 4th-order for numerical time integration. For pure capillary waves and gravity-capillary waves, it was found that MEL could be numerically unstable even with filtering. On the other hand, the results have shown that UHT is more stable and produces highly accurate solutions without filtering.

The generation of parasitic capillary waves is successfully computed using UHT even without filtering. Note that both methods could numerically model the initial stage of the generation of parasitic capillary waves, but MEL fails to continue accurate computation beyond the initial stage. As remarked by Boyd [6], we should notice that the filtering technique should not be used, if possible, for reliable computing. From our numerical results, we may conclude that, compared with MEL, UHT has some merits in numerical stability, accuracy and reliability.

In addition to the linear stability considered in section 4, the difference between the two methods is partially due to the clustering property of the sample points on the free surface as discussed in section 7. Comparison of the sample point distribution suggested that, from the point of view of spatial resolution on the free surface, MEL is suitable for gravity dominated waves and UHT for capillary dominated waves.

Acknowledgements

The authors thank anonymous reviewers for their valuable comments. W.C. gratefully acknowledges support from the National Research Foundation of Korea grant funded by the Korea government (MSIP) through GCRC-SOP (No. 2011-0030013) for his visit to the Pusan National University as a visiting professor, and the US National Science Foundation through Grant No. DMS-1517456.

Appendix A. Energies of gravity-capillary water waves

Each energy of gravity-capillary water waves can be written in the dimensional form using the complex coordinate $Z^* = X^* + \mathrm{i}Y^*$ and the complex velocity $W^* = \partial F^*/\partial Z^* = U^* - \mathrm{i}V^*$ in the inertial frame as

$$\begin{cases} E_{\mathrm{K}}^*(t) = \displaystyle\iint_{\mathcal{D}^*} \frac{1}{2}\rho(U^{*2} + V^{*2})\mathrm{d}X^*\mathrm{d}Y^* \ , \\ E_{\mathrm{P}}^*(t) = \displaystyle\int_{X_{\mathrm{A}}^*}^{X_{\mathrm{B}}^*}\int_0^{\eta^*} \rho g Y^*\mathrm{d}Y^*\mathrm{d}X^* \ , \\ E_{\mathrm{S}}^*(t) = T\left(\displaystyle\int_{\mathcal{S}^*} \mathrm{d}s^* - \lambda\right) \ , \end{cases} \tag{A.1}$$

where $\mathcal{D}^*$ is the flow domain, X_{A}^* and X_{B}^* are the X^* coordinates of the points A and B shown in Fig. 1(a), $\mathcal{S}^* : Y^* = \eta^*(X^*, t)$ is the free surface and $\mathrm{d}s^* = \sqrt{\mathrm{d}X^{*2} + \mathrm{d}Y^{*2}}$. We can obtain these energies in the non-dimensional form using UHT in the frame of reference moving with waves as follows:

(i) The case of $F_\lambda > 0$

$$\begin{cases} E_{\rm K}(t) = \dfrac{E_{\rm K}^*(t)}{\rho g \lambda^3} = -\dfrac{1}{2}\left(\dfrac{F_\lambda}{2\pi}\right)^2 \displaystyle\int_{-\pi}^{\pi} (\psi - y)(\phi_\sigma - x_\sigma)\mathrm{d}\sigma \ , \\ E_{\rm P}(t) = \dfrac{E_{\rm P}^*(t)}{\rho g \lambda^3} = -\dfrac{1}{2}\dfrac{1}{(2\pi)^3} \displaystyle\int_{-\pi}^{\pi} y^2 x_\sigma \mathrm{d}\sigma \ , \\ E_{\rm S}(t) = \dfrac{E_{\rm S}^*(t)}{\rho g \lambda^3} = \dfrac{1}{2\pi}\dfrac{{F_\lambda}^2}{W_e} \displaystyle\int_{-\pi}^{\pi} (\sqrt{{x_\sigma}^2 + {y_\sigma}^2} - 1)\mathrm{d}\sigma \ . \end{cases} \tag{A.2}$$

(ii) The case of $F_\lambda = 0$ (pure capillary waves)

$$\begin{cases} E_{\rm K}(t) = \dfrac{E_{\rm K}^*(t)}{T\lambda} = -\dfrac{1}{2}\dfrac{W_e}{(2\pi)^2} \displaystyle\int_{-\pi}^{\pi} (\psi - y)(\phi_\sigma - x_\sigma)\mathrm{d}\sigma \ , \\ E_{\rm P}(t) = \dfrac{E_{\rm P}^*(t)}{T\lambda} = 0 \ , \\ E_{\rm S}(t) = \dfrac{E_{\rm S}^*(t)}{T\lambda} = \dfrac{1}{2\pi} \displaystyle\int_{-\pi}^{\pi} (\sqrt{{x_\sigma}^2 + {y_\sigma}^2} - 1)\mathrm{d}\sigma \ . \end{cases} \tag{A.3}$$

By changing σ to $-\alpha$ in (A.2) and (A.3), we can get the equations for these energy in MEL.

References

[1] G. Baker, D. Meiron, S. Orszag, Generalized vortex methods for free-surface flow problems, J. Fluid Mech. 123 (1982) 477–501.
[2] G. Baker, A. Nachbin, Stable methods for vortex sheet motion in the presence of surface tension, SIAM J. Sci. Comput. 19 (1998) 1737–1766.
[3] G. Baker, C. Xie, Singularities in the complex physical plane for deep water waves, J. Fluid Mech. 685 (2011) 83–116.
[4] J. Beale, T. Hou, J. Lowengrub, Convergence of a boundary integral method for water waves, SIAM J. Numer. Anal. 33 (1996) 1797–1843.
[5] J. Beale, T. Hou, J. Lowengrub, M. Shelley, Spatial and temporal stability issues for interracial flows with surface tension, Math. Comput. Model. 20 (1994) 1–27.
[6] J. Boyd, Chebyshev and Fourier Spectral Methods, 2nd edition, Dover, 2001.
[7] C. Canuto, M. Hussaini, A. Quarteroni, T. Zang, Spectral Methods in Fluid Dynamics, Springer-Verlag, 1986.
[8] H. Ceniceros, T. Hou, Convergence of a non-stiff boundary integral method for interfacial flows with surface tension, Math. Comput. 67 (1998) 137–182.
[9] D. Chalikov, D. Sheinin, Modeling extreme waves based on equations of potential flow with a free surface, J. Comput. Phys. 210 (2005) 247–273.
[10] B. Chen, P. Saffman, Steady gravity-capillary waves on deep water – I. Weakly nonlinear waves, Stud. Appl. Math. 60 (1979) 183–210.
[11] B. Chen, P. Saffman, Steady gravity-capillary waves on deep water – II. Numerical results for finite amplitude, Stud. Appl. Math. 62 (1980) 95–111.
[12] W. Choi, Nonlinear surface waves interacting with a linear shear current, Math. Comput. Simul. 80 (2009) 29–36.
[13] W. Choi, R. Camassa, Exact evolution equations for surface waves, J. Eng. Mech. 125 (1999) 756–760.
[14] C. Cox, Measurements of slopes of high-frequency wind waves, J. Mar. Res. 16 (1958) 199–225.
[15] G. Crapper, An exact solution for progressive capillary waves of arbitrary amplitude, J. Fluid Mech. 2 (1957) 532–540.
[16] T. Davies, The theory of symmetrical gravity waves of finite amplitude. I, Proc. R. Soc. Lond. A 208 (1951) 475–486.
[17] F. Dias, T. Bridges, The numerical computation of freely propagating time-dependent irrotational water waves, Fluid Dyn. Res. 38 (2006) 803–830.
[18] J. Dold, An efficient surface-integral algorithm applied to unsteady gravity waves, J. Comput. Phys. 103 (1992) 90–115.
[19] D. Dommermuth, Efficient simulation of short and long-wave interactions with applications to capillary waves, J. Fluids Eng. 116 (1994) 77–82.
[20] D. Dommermuth, D. Yue, W. Lin, R. Rapp, E. Chan, W. Melville, Deep-water plunging breakers: a comparison between potential theory and experiments, J. Fluid Mech. 189 (1988) 423–442.
[21] A. Dyachenko, E. Kuznetsov, M. Spector, V. Zakharov, Analytical description of the free surface dynamics of an ideal fluid (canonical formalism and conformal mapping), Phys. Lett. A 221 (1996) 73–79.
[22] N. Ebuchi, H. Kawamura, Y. Toba, Fine structure of laboratory and wind-wave surfaces studied using an optical method, Bound.-Layer Meteorol. 39 (1987) 133–151.
[23] A. Fedorov, W. Melville, Nonlinear gravity-capillary waves with forcing and dissipation, J. Fluid Mech. 354 (1998) 1–42.
[24] A. Fedorov, W. Melville, A. Rozenberg, An experimental and numerical study of parasitic capillary waves, Phys. Fluids 10 (1998) 1315–1323.
[25] T. Hou, Numerical solutions to free boundary problems, Acta Numer. 4 (1995) 335–415.
[26] T. Hou, J. Lowengrub, M. Shelley, Removing the stiffness from interfacial flows with surface tension, J. Comput. Phys. 114 (1994) 312–338.
[27] L.-P. Hung, W.-T. Tsai, The formation of parasitic capillary ripples on gravity-capillary waves and the underlying vortical structures, J. Phys. Oceanogr. 39 (2009) 263–289.
[28] L. Jiang, H.-J. Lin, W. Schultz, M. Perlin, Unsteady ripple generation on steep gravity-capillary waves, J. Fluid Mech. 386 (1999) 281–304.
[29] Y. Li, J. Hyman, W. Choi, A numerical study of the exact evolution equations for surface waves in water of finite depth, Stud. Appl. Math. 113 (2004) 303–324.
[30] M. Longuet-Higgins, The generation of capillary waves by steep gravity waves, J. Fluid Mech. 16 (1963) 138–159.

[31] M. Longuet-Higgins, Parasitic capillary waves: a direct calculation, J. Fluid Mech. 301 (1995) 79–107.
[32] M. Longuet-Higgins, E. Cokelet, The deformation of steep surface waves on water, I. A numerical method of computation, Proc. R. Soc. Lond. A 350 (1976) 1–26.
[33] D. Meiron, S. Orszag, M. Israeli, Applications of numerical conformal mapping, J. Comput. Phys. 40 (1981) 345–360.
[34] R. Mui, D. Dommermuth, The vortical structure of parasitic capillary waves, J. Fluids Eng. 117 (1995) 355–361.
[35] H. Okamoto, M. Shōji, The Mathematical Theory of Permanent Progressive Water-Waves, World Scientific, 2001.
[36] L. Ovshannikov, To the shallow water theory foundation, Arch. Mech. 26 (1974) 407–422.
[37] M. Perlin, W. Choi, Z. Tian, Breaking waves in deep and intermediate waters, Annu. Rev. Fluid Mech. 45 (2013) 115–145.
[38] M. Perlin, H. Lin, C.-L. Ting, On parasitic capillary waves generated by steep gravity waves: an experimental investigation with spatial and temporal measurements, J. Fluid Mech. 255 (1993) 597–620.
[39] M. Perlin, W. Schultz, Capillary effects on surface waves, Annu. Rev. Fluid Mech. 32 (2000) 241–274.
[40] W. Schultz, J. Huh, O. Griffin, Potential energy in steep and breaking waves, J. Fluid Mech. 278 (1994) 201–228.
[41] L. Schwartz, J. Fenton, Strongly nonlinear waves, Annu. Rev. Fluid Mech. 14 (1982) 39–60.
[42] L. Schwartz, J.-M. Vanden-Broeck, Numerical solution of the exact equations for capillary-gravity waves, J. Fluid Mech. 95 (1979) 111–139.
[43] A. Sidi, M. Israeli, Quadrature methods for periodic singular and weakly singular Fredholm integral equations, J. Sci. Comput. 3 (1988) 201–231.
[44] D. Skyner, A comparison of numerical predictions and experimental measurements of the internal kinematics of a deep-water plunging wave, J. Fluid Mech. 315 (1996) 51–64.
[45] S. Tanveer, Singularities in water waves and Rayleigh–Taylor instability, Proc. R. Soc. Lond. A 435 (1991) 137–158.
[46] S. Tanveer, Singularities in the classical Rayleigh–Taylor flow: formation and subsequent motion, Proc. R. Soc. Lond. A 441 (1993) 501–525.
[47] R. Tiron, W. Choi, Linear stability of finite-amplitude capillary waves on water of infinite depth, J. Fluid Mech. 696 (2012) 402–422.
[48] W.-T. Tsai, D. Yue, Computation of nonlinear free-surface flows, Annu. Rev. Fluid Mech. 28 (1996) 249–278.
[49] J.-M. Vanden-Broeck, Gravity-Capillary Free-Surface Flows, Cambridge University Press, Cambridge, 2010.
[50] T. Vinje, P. Brevig, Numerical simulation of breaking waves, Adv. Water Resour. 4 (1981) 77–82.
[51] H. Yamada, Permanent gravity waves on water of uniform depth, Rep. Res. Inst. Appl. Mech. 6 (1958) 127–139.